



# Enhanced optical properties and localized surface plasmon resonance of magnetite/silver nanocomposites under electric field and wavelength variation

Muhammad Riswan<sup>1</sup> · Eri Widiyanto<sup>2</sup> · Hervin Maulina<sup>1,3</sup> · Muhammad Arifin<sup>1</sup> · Iman Santoso<sup>1</sup> · Edi Suharyadi<sup>1</sup> 

Received: 5 January 2025 / Accepted: 26 March 2025  
© Qatar University and Springer Nature Switzerland AG 2025

## Abstract

The study of optical properties and localized surface plasmon resonance (LSPR) of magnetite/silver nanocomposites (NCs) has been successfully investigated. The NCs were synthesized using the co-precipitation method and coated on the Au film surface with a four-layer Kretschmann configuration system. Light source wavelengths of 405 and 450 nm were used to investigate the influence of the varied wavelength on the optical properties and LSPR curve characteristics. Electric fields of 1.6, 2.4, and 3.2 V/cm were applied to the substrate/Au film/magnetite/silver NCs/air sample structure for ellipsometer and SPR testing. The findings indicate that the use of an electric field improves the optical properties, a real part of optical conductivity  $\sigma_1$ , complex dielectric constant (real part,  $\epsilon_1$  and imaginary part,  $\epsilon_2$ ), complex refractive index (real part,  $n$  and imaginary part,  $k$ ), and optical absorption ( $\alpha$ ), resulting in a rise in the LSPR angle and a decrease in minimum reflectance. Furthermore, the variation in the incident light wavelength at 405, 450, and 632.8 nm causes an increase in the LSPR angle by 1.21°, 0.97°, and 0.66°, respectively. At a wavelength of 405 nm, the application of electric fields of 1.6, 2.4, and 3.2 V/cm induced shifts in the LSPR angle from 65.87° to 65.99°, 66.23°, and 66.49°, respectively. At 450 nm, the LSPR angle shifted from 63.41° to 63.62°, 63.77°, and 63.94°, respectively. The significant change in the LSPR angle and minimum reflectance due to the applied electric field and wavelength indicates that applying an electric field to the LSPR sensor surface with varied wavelengths provides the scenario to improve the performance of the SPR biosensor for future applications.

**Keywords** Au thin film · Magnetite/silver nanocomposite · Optical properties · Surface plasmon resonance · Spectroscopic ellipsometry

## 1 Introduction

Nanoscience and nanotechnology are the latest breakthroughs in science and technology that have exhibited rapid development in recent decades. Materials at the nanoscale exhibit behaviour that is intermediate between macroscopic solids and atomic systems due to quantum confinement effects, electrodynamic interactions, and the high surface-to-volume ratio [1, 2]. Noble metal nanoparticles, such as silver (Ag) and gold (Au), display surface plasmon resonance (SPR) phenomena [3, 4]. These phenomena refer to light absorption enhancement and scattering around the plasmon resonance peak. In addition, the position and intensity of the plasmon resonance in the absorption spectrum are significantly influenced by the shape, size, and medium in which the nanoparticles are embedded [5]. SPR has been

✉ Edi Suharyadi  
esuharyadi@ugm.ac.id

<sup>1</sup> Department of Physics, Universitas Gadjah Mada, Sekip Utara, Yogyakarta 55281, Indonesia

<sup>2</sup> Department of Physics, Faculty of Engineering, Universitas Singaperbangsa Karawang, Telukjambe Timur, Karawang 41361, Indonesia

<sup>3</sup> Department of Physics Education, Faculty of Teacher Training and Education, Universitas Lampung, Lampung 35145, Indonesia

widely utilized in various fields, including biosensing [6], photothermal therapy [7], diagnostics [8] etc. SPR marks an advance in optical biosensor technology, with the advantages of real-time testing, label-free detection, fast response time [9], and non-destructive measurement [10]. These advantages contribute to its effectiveness in detecting organic analytes, especially in the fields of drug screening [9], clinical diagnosis [11], and food quality control [12]. SPR is a collective oscillation of electrons induced by electromagnetic waves at the interface of materials exhibiting opposite permittivity, commonly observed in metals and dielectrics [13, 14]. It occurs when p-polarized light at a specific wavelength is directed onto a metal-coated prism at a particular angle, generating surface plasmons (SP) [15] through electromagnetic waves, known as evanescent waves, at the metal-dielectric interface. These evanescent waves decay exponentially across the boundary, fading within approximately 200 nm of the sensor surface. Resonance is achieved when the propagation constant of the evanescent wave is equal to the propagation constant of the SP [16, 17], where the physical parameter of the resonance can be identified by observing the reduction in reflected light intensity at a defined angle called the SPR angle [18–20], which depends on the refractive index of the prism, the dielectric constant of the metal, and the detected material [21, 22].

SPR with a Kretschmann configuration system consisting of a prism, metal thin film, and air has weakness in detecting biomolecules with tiny sizes and refractive index [22, 23]. Modifications are needed to increase the sensitivity of the SPR biosensor. One of the modifications that can be performed is by adding the nanoparticles (NPs) [24, 25]. NPs in composite structures, commonly referred to as nanocomposites (NCs), composed of two or more materials, such as metals and semiconductors, have attracted the attention of researchers in recent years due to their unique properties, including composition versatility, good stability, monodispersity, and self-assembling ability. Metal/semiconductor NCs exhibit a strong exciton coupling effect between the SPR phenomena of metal nanoparticles and semiconductor excitons, enhancing their applicability in SPR-related applications. Among various inorganic semiconductor nanoparticles, magnetite ( $\text{Fe}_3\text{O}_4$ ) is of interest to research due to its size-dependent electronic and optical properties. Additionally, their widespread availability and significant utility in immobilizing and purifying biomolecules in SPR sensors highlight several key advantages. Firstly, its outstanding magnetic properties allow direct capture of target molecules. Secondly, the large surface area allows high-density immobilization of biomolecules; and thirdly, its high molecular weight and refractive index enhance the SPR signal, making them very suitable as an active material in SPR-based applications [26]. Furthermore, magnetite in the nanoparticle

scale with a specific size exhibits superparamagnetic characteristics that can increase the effective mass on the surface of SPR sensors [22, 23, 27, 28]. In addition, the high reactivity of iron (Fe) atoms in magnetite enables easy functionalization with additional materials. However, magnetite NPs are easily oxidized, which reduces their chemical and physical stability and decreases their magnetic properties [24, 25, 29–33].

These challenges can be overcome by combining magnetite with noble metals such as Ag in magnetite/silver NCs. Ag exhibits good chemical stability, flexibility, and easy functionalization with other materials [34], such as magnetite nanoparticles [35]. In addition, Ag nanoparticles demonstrate low optical loss in the visible spectrum and possess a negative real dielectric constant [36], which enables localized surface plasmon resonance (LSPR) effect when they interact with light [37]. The LSPR effect can strongly confine the electromagnetic field, while significantly amplifying the local electric field near the metal surface. It is influenced by factors, such as the dielectric environment, the size of the nanomaterials, and their composition [38–40]. Magnetite/silver NCs have significant potential for various applications as they combine the unique properties of metals and semiconductors, leading to the emergence of new electrical and optical characteristics through the synergistic interactions between the metal and semiconductor components [41]. Thus, the surface modification of magnetite NPs with Ag NPs to form a magnetite/silver NCs structure provides a scenario to enhance the stability of the nanoparticle in solution, improve their dispersibility, generate plasmonic effects, and amplify SPR signals [42–44].

On the other hand, the SPR curve characteristics, including SPR angle, reflectance, and full width at half maximum, are strongly affected by the dielectric constant of the prism, metal, and detected material, as well as the wavelength of the incident light. Metals have free electrons that follow the Drude dielectric function model, where modifications to their dielectric constant influence the optical response and the coupling point between the evanescent wave vector and the surface plasmon wave vector, resulting in changes to the characteristic surface plasmon resonance (SPR) curve [42]. The dielectric constant can be manipulated by applying an electric field to the sensing surface, which utilizes the electro-optic effect. When a low-frequency electric field is applied, free electrons in the metal redistribute, leading to a surface charge density (charge per unit surface area), which causes the change in the number of free electrons per unit area of the surface, modifying the dielectric function of the metals, which in turn changes the coupling points of the surface plasmon and evanescent wave vectors. As a result, there are observable changes in the SPR angle and the minimum reflectance [45]. Moreover, applying electric

fields causes alterations in the charge carriers, thereby generating active plasmons capable of amplifying the detection signal of the SPR biosensor [45]. Some previous research has been performed on the application of electric fields for LSPR applications. Enhancing SPR spectroscopy with electric fields offers a promising approach to advancing fundamental research and enabling new applications for SPR sensors, leading to greater sensitivity than traditional SPR techniques [46].

On the other hand, other modifications to improve the performance of SPR biosensors can be achieved by varying the wavelength of the light source [47–49]. Altering the light source's wavelength modifies the coupling point between the evanescent wave and the surface plasmon wave, consequently changing the SPR angle. Therefore, combining an electric field with magnetite/silver NCs as an active material with varied wavelengths enhances the potential of EO-modulated biosensors to exhibit superior sensitivity compared to conventional SPR biosensors. We recently reported the impact of varying electric fields on the LSPR characteristics of magnetite/silver NCs using a light source wavelength of 632.8 nm [50]. Applying the electric field increased the SPR angle and minimum reflectance; a higher electric field resulted in larger SPR angle and minimum reflectance values. In this study, we conducted continuous research by investigating the changes in the optical properties and LSPR of magnetite/silver NCs by applying an electric field and light source variation. Modulating the wavelength changes the displacement of the coupling point between evanescent waves and surface plasmon waves, which results in a shift of the SPR angle. This phenomenon is due to the real and imaginary components of the wavelength-dependent dielectric constant of the NCs, which induces changes in the optical response [45].

Therefore, the objective of this study is to explore how varying the electric field and incident light wavelength influences the optical properties and LSPR characteristics of magnetite/silver NCs. This research demonstrates how these two factors can enhance the performance of magneto-plasmonic NCs. The novelty of this research lies in the comprehensive analysis of how the electric field and wavelength variation can simultaneously affect both the optical and plasmonic properties of magnetite/silver NCs. Additionally, this study provides insight into how the manipulation of both electric field and light wavelength can shift the LSPR characteristics, such as the LSPR angle and minimum reflectance [51, 52]. These changes are significant because they directly impact the sensitivity and performance of SPR sensors. Therefore, by understanding these correlations, the research opens the door to developing more efficient and sensitive biosensors, which could have applications that can be utilized in various fields of technology. This study seeks

to enhance the fundamental understanding of magnetite/silver NCs' optical and plasmonic properties and demonstrates how these insights could be leveraged to improve SPR biosensor technology.

## 2 Experimental details

### 2.1 Reagents

The materials used in this study include  $\text{FeSO}_4 \cdot 7\text{H}_2\text{O}$ ,  $\text{FeCl}_3 \cdot 6\text{H}_2\text{O}$ ,  $\text{AgNO}_3$ , APTMS (97%), ethanol (96%), and aqueous ammonia (25%). All chemicals for nanoparticle synthesis were analytical grade and purchased from Merck (Germany) and Aldrich (USA).

### 2.2 Synthesis of magnetite/silver NCs

The synthesis of NCs is carried out in three stages. In the first stage, magnetite NPs are synthesized via co-precipitation, using ( $\text{FeSO}_4 \cdot 7\text{H}_2\text{O}$ ) and ( $\text{FeCl}_3 \cdot 6\text{H}_2\text{O}$ ) as Fe ion sources in a 1:2 molar ratio, with  $\text{NH}_4\text{OH}$  acting as the reducing agent. A solution of 4.170 g of ( $\text{FeSO}_4 \cdot 7\text{H}_2\text{O}$ ) and 8.109 g of ( $\text{FeCl}_3 \cdot 6\text{H}_2\text{O}$ ) in 15 mL of water is mixed using a magnetic stirrer, while 36 mL of pure water dissolves 24 mL of  $\text{NH}_4\text{OH}$  for 15 min. The  $\text{NH}_4\text{OH}$  solution is slowly added to the previous solution for about 90 min, maintaining constant stirring at 450 rpm and a temperature of  $\sim 60^\circ\text{C}$ . The solution was dark in colour, washed, and dried at  $80^\circ\text{C}$  for 2 h to yield magnetite NPs, as shown in Fig. 1(a). In the second stage, magnetite NPs are functionalized with  $\text{C}_6\text{H}_7\text{NO}_3\text{Si}$  (APTMS) as a linker between magnetite and silver NPs. A mixture of 500 mg of magnetite NPs, 10 mL of APTMS, 200 mL of ethanol, and 10 mL of  $\text{NH}_4\text{OH}$  is sonicated for 60 min at room temperature, then cleaned and dried at  $70^\circ\text{C}$  for 2 h as shown in Fig. 1(b). In the final stage, a mixture of magnetite NPs-APTMS, 20 mM  $\text{AgNO}_3$ , and 400 mL of ethanol is stirred for 4 h at ambient temperature. The magnetite/silver NCs are separated from the solution using a permanent magnet and dried at  $70^\circ\text{C}$  for 2 h, as illustrated in Fig. 1(c).

### 2.3 Characterization and sample preparation

X-ray diffraction (XRD) analysis was performed to identify the crystalline phase of the nanoparticles. The magnetic properties of the NPs were evaluated using a vibrating sample magnetometer (VSM), and transmission electron microscopy (TEM) and energy-dispersive X-ray spectroscopy (EDX) were used to examine the morphology and elemental composition of the NPs.

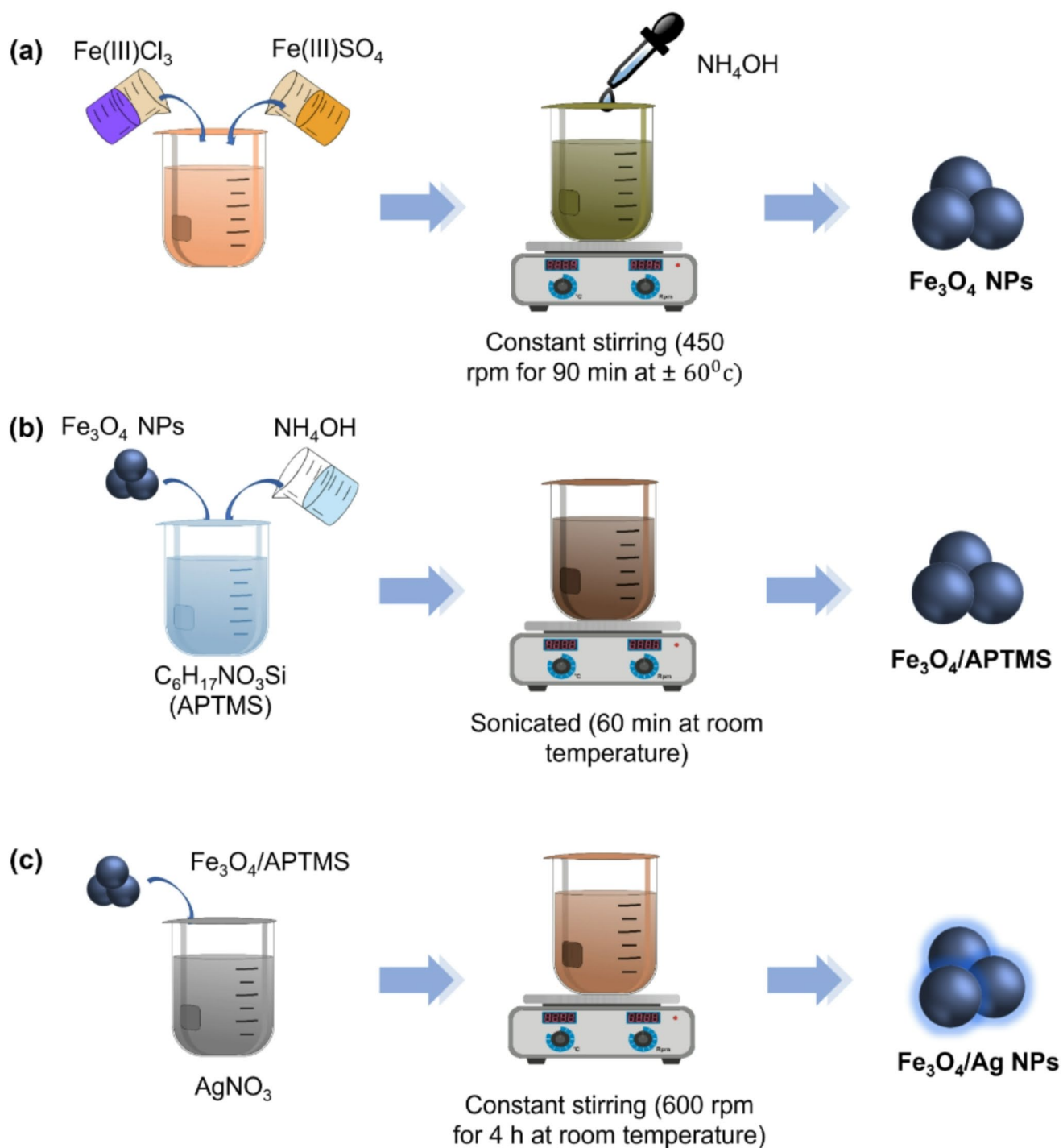


**Fig. 1** Synthesis scheme of magnetite/silver NCs, including (a) synthesis process of magnetite NPs, (b) surface modification of the magnetite NPs utilizing APTMS, and (c) deposition of Ag NPs on magnetite/APTMS NPs

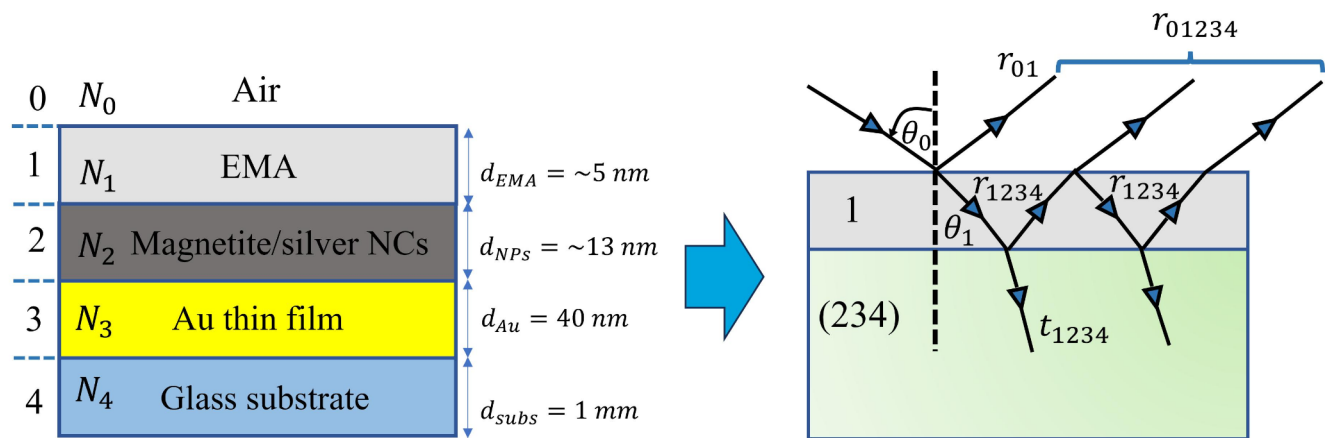


**Fig. 2** Schematic diagram of the five-layer multilayer optical model (Air/EMA/magnetite/silver NCs/Au Film/glass substrate) with a refractive index of  $N_0$ ,  $N_1$ ,  $N_2$ ,  $N_3$ , and  $N_4$  respectively.

$d_{EMA}$ ,  $d_{NPs}$ ,  $d_{Au}$ , and  $d_{subs}$  are the thickness of EMA, NCs, Au, and substrate, and  $r_{1234}$  and  $t_{1234}$  are reflectance and transmittance of the layers [55]

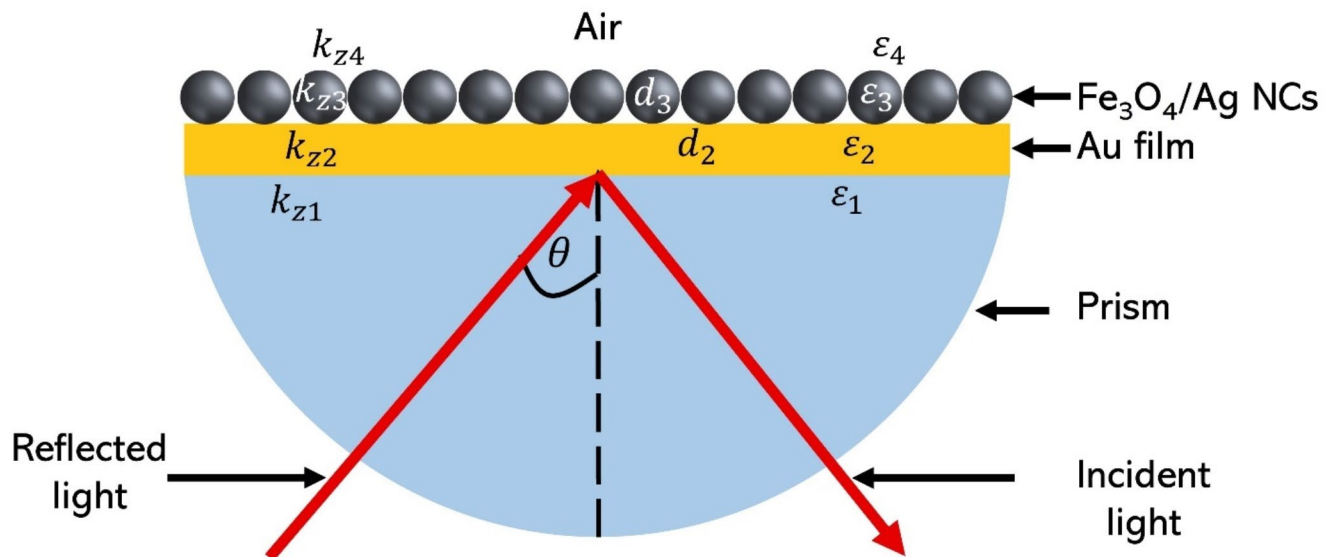


**Fig. 3** Schematic diagram illustrating the Kretschmann array with layer structure of prism/Au film/magnetite/silver NCs/air [53]

To perform optical properties and SPR testing, 0.025 g of Au was evaporated on the top of the glass substrate to form a glass substrate/Au film structure. The NCs were deposited on the surface of the Au film utilizing a spray method to form glass substrate/Au film/NCs for optical property measurements using spectroscopic ellipsometry. A similar process was performed for the SPR test but using a half-cylindrical prism substrate. The Au film thickness was approximately 40 nm, as reported in previous studies [53].

#### 2.4 Multilayer system structure

The ellipsometer examination was conducted on a five-layered structure comprising a glass substrate, an Au film, NCs, and air serving as the dielectric medium. Figure 2 displays

the optical model of the multilayer structure to depict the sample configuration [54]. Figure 3. Illustrates the multilayer structure utilizing the Kretschmann array to measure the SPR characteristics comprising a prism, Au film, magnetite/silver NCs, and air. Symbol notation is described in the subsequent discussion.

#### 2.5 Optical properties measurements

The optical properties measurement was performed utilizing a homemade rotating analyzer ellipsometer (RAE), as shown in Fig. 4. The RAE components have been reported in detail in previous studies [56]. The measurement was carried out using the incident angle of  $75^\circ$  and the polarization angle of  $45^\circ$ . The electric field was applied on the sample

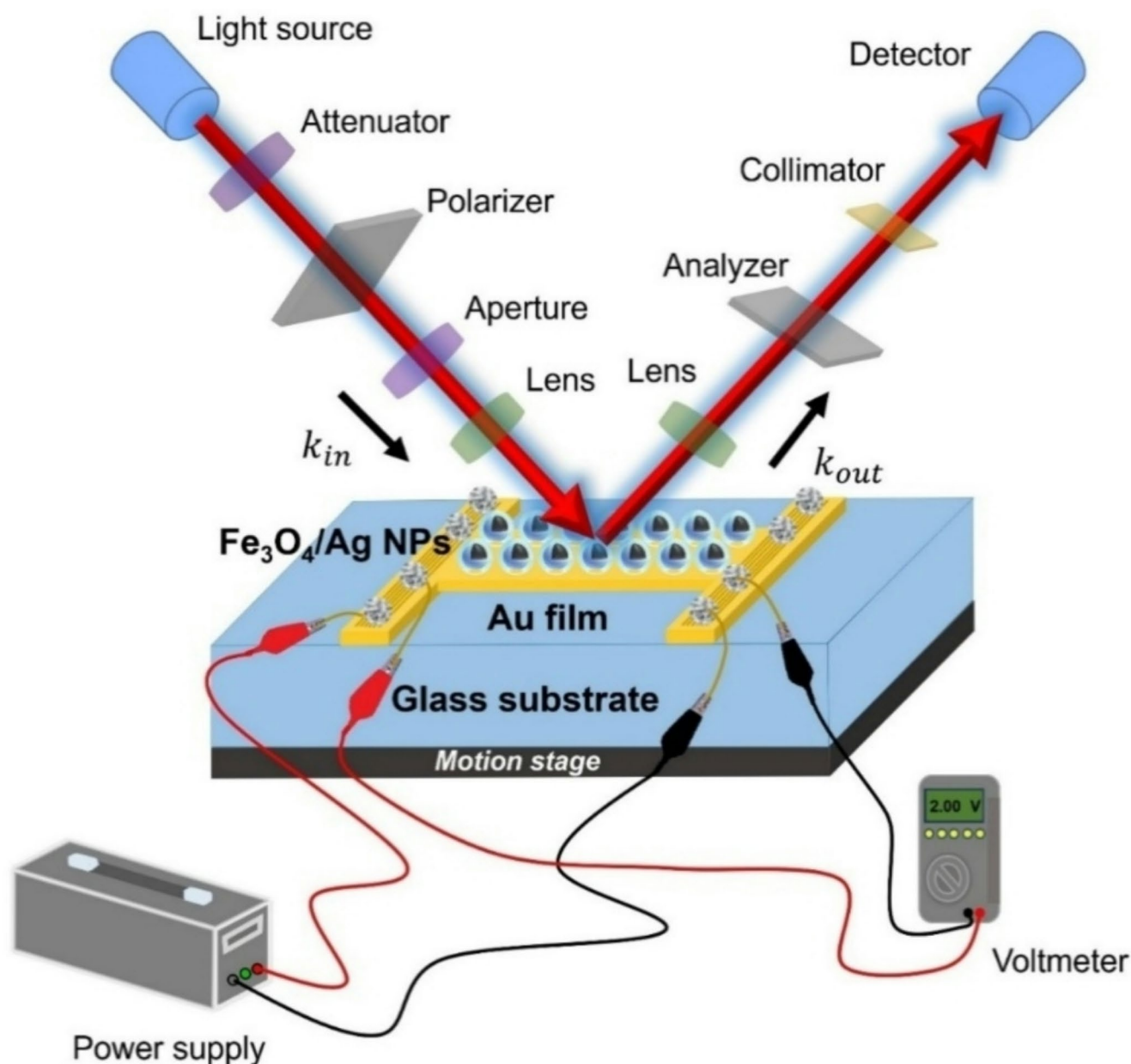


**Fig. 4** Rotating Analyzer Ellipsometer (RAE) setup under an electric field. The voltage from the power supply is induced to the Au surface using a single wire, while a voltmeter reads the incoming voltage on the Au thin film

**Table 1** Variations in electric voltage, electric current, and electric field induced to the surface of the multilayer structure

No	Electric Voltage (Volt)	Electric Current (A)	Electric Field (V/cm)
1	0	0	0
2	2	0.44	1.6
3	3	0.63	2.4
4	4	0.75	3.2

surface through the electric voltages of 2, 3, and 4 V generated by a Keithley source. The silver paste was used as an electrode to attach the single wire to the sample surface. The details about the electric field, voltage, and current are attached in Table 1.

The measurement was performed on the following sample structures: sample 1 ( $S_1$ ), consisting of a glass substrate/Au film; sample 2 ( $S_2$ ), comprising a glass/substrate/Au film/magnetite/silver NCs; and samples 3, 4, and 5 ( $S_3$ ,  $S_4$ , and  $S_5$ ) consist of a glass/substrate/Au film/magnetite/silver NCs with varying electric field strengths of 1.6, 2.4, and 3.2 V/cm, respectively. The  $\psi$  and  $\Delta$  values obtained from

the measurements were investigated using IGOR Pro 7 software to develop the precise optical model for determining the optical properties of the material, including optical conductivity, refractive index, dielectric constant, and absorption coefficient. The fitting process was completed until the root mean square error followed the standards. The relationship between the parameters of  $\psi$  and  $\Delta$  and the optical properties is formulated as [57, 58]:

$$\rho \equiv \tan(\psi) \exp(i\Delta) \equiv \frac{r_{,01,234,p}}{r_{,01,234,s}} \quad (1)$$

where  $r_{,01,234,p}$  and  $r_{,01,234,s}$  represent the reflection coefficients of  $p(s)$  polarized light of the five-layer optical model.  $\tan \psi$  is equal to the absolute value of the ratio of the reflection coefficients of p- and s-polarized light. The angle  $\Delta$  varies from  $0^\circ$  to  $90^\circ$ . The p and s-polarization are in phase due to RAE, and the incident light is linearly polarized. After reflection, the phases may alter because of the characteristics of the complex refractive index and optical interference in multilayer thin films.  $r_{,01,234}$  and  $r_{,01,234}$  are expressed as [57, 58]:

$$r_{,012,34} = \frac{r_{01} + r_{1234} \exp(-i2\beta_1)}{1 + r_{01} r_{1234} \exp(-i2\beta_1)} \quad (2)$$

$$r_{1234} = \frac{r_{12} + (r_{23} + r_{34} \exp(-i2\beta_3)) \exp(-i2\beta_2)}{1 + r_{12} (1 + r_{23} r_{34} \exp(-i2\beta_3)) \exp(-i2\beta_2)} \quad (3)$$

where  $\beta_1 = (2\pi d_1 \sqrt{\epsilon_1 - \epsilon_0 \sin^2 \theta_0}) / \lambda$ ,  $\beta_2 = (2\pi d_2 \sqrt{\epsilon_2 - \epsilon_0 \sin^2 \theta_0}) / \lambda$ , and  $\beta_3 = (2\pi d_3 \sqrt{\epsilon_3 - \epsilon_0 \sin^2 \theta_0}) / \lambda$ . Meanwhile,  $d_1$ ,  $d_2$ , and  $d_3$  is the thicknesses of the EMA layer, magnetite/silver NCs layer, and Au thin film. Meanwhile,  $\epsilon_1$ ,  $\epsilon_2$ , and  $\epsilon_3$  symbolize their complex dielectric constants, respectively. The reflectivity coefficients of layers can be obtained employing the Fresnel formulation as follows [57, 58]:

$$r_{mn,p} = \frac{\sqrt{\frac{\epsilon_n}{\epsilon_m} (\epsilon_m - \epsilon_0 \sin^2 \theta_0)^{1/2}} - \sqrt{\frac{\epsilon_m}{\epsilon_n} (\epsilon_n - \epsilon_0 \sin^2 \theta_0)^{1/2}}}{\sqrt{\frac{\epsilon_n}{\epsilon_m} (\epsilon_m - \epsilon_0 \sin^2 \theta_0)^{1/2}} + \sqrt{\frac{\epsilon_m}{\epsilon_n} (\epsilon_n - \epsilon_0 \sin^2 \theta_0)^{1/2}}} \quad (4)$$

$$r_{mn,s} = \frac{(\epsilon_m - \epsilon_0 \sin^2 \theta_0)^{1/2} - (\epsilon_n - \epsilon_0 \sin^2 \theta_0)^{1/2}}{(\epsilon_m - \epsilon_0 \sin^2 \theta_0)^{1/2} + (\epsilon_n - \epsilon_0 \sin^2 \theta_0)^{1/2}} \quad (5)$$

where m and n are consecutive indices, the fitting process involves aligning the  $\psi$  and  $\Delta$  data with the appropriate model to obtain the best match. Specifically, the Cauchy model is suitable for the transparent materials employed in this investigation, such as glass. This model is defined as [55]:

$$N = A + \frac{B}{\lambda^2} + \frac{C}{\lambda^4} + \dots ; k = 0 \quad (6)$$

where A, B, and C represent fitting parameters. These parameters remain constant for each thickness, with only the Drude-Lorentz parameters being adjusted.

The free parameters are the oscillator peak corresponding to the plasma frequency ( $\omega_p$ ), the transfer frequency corresponding to the peak position ( $\omega_0$ ), the oscillator width ( $\Gamma$ ), the Au film thickness ( $d_2$ ), and glass substrate thickness ( $d_3$ ). The Drude-Lorentz model for metal materials is used to model the Au film and the NCs, the Cauchy dispersion model is for glass substrate, and Bruggeman's EMA theory [59] was used to model the roughness of the Au, consisting of 50% Au and 50% air [55, 60, 61]. The extraction of optical properties involves modelling and comparing the experimental data obtained by adjusting several parameters, such as optical constant and thickness. The values closest to the experimental results are determined during this iteration procedure by reducing the mean square error ( $\chi^2$ ) of the modelled data [57].

$$\chi^2 = \chi_{psi}^2 + \chi_{del}^2 \quad (7)$$

$$\chi^2 = \frac{1}{\sqrt{M-P-1}} \left\{ \sum_{j=1}^M \left[ \frac{\psi_{exp}(\omega_j) - \psi_{cal}(\omega_j)}{\delta \psi(\omega_j)} \right]^2 + \left[ \frac{\Delta_{exp}(\omega_j) - \Delta_{cal}(\omega_j)}{\delta \Delta(\omega_j)} \right]^2 \right\} \quad (8)$$

where  $M$  and  $P$  represent the number of data and parameters, respectively;  $\psi_{exp}$  and  $\psi_{cal}$  denote  $\psi$  from experiment and calculation, respectively;  $\Delta_{exp}$  and  $\Delta_{cal}$  are  $\Delta$  from experiment and calculation at a certain frequency  $\omega_j$ , respectively;  $\delta \psi$  and  $\delta \Delta$  correspond to the measurement error in ( $\psi$ ,  $\Delta$ ). The Drude-Lorentz formulation can be calculated as follows [54]:

$$\epsilon(\omega) = \epsilon_\infty + \sum_{k=1}^N \frac{\omega_{p,k}^2}{\omega_{0,k}^2 - \omega^2 - i\omega \Gamma_k} \quad (9)$$

where  $\epsilon_\infty$  signifies the high-frequency dielectric constant. The parameters  $\omega_0$ ,  $\omega_p$ ,  $\Gamma_k$  denote the transverse frequency (eigenfrequency), plasma frequency, and line width (scattering rate) of the  $k_{th}$  oscillator. The EMA Bruggeman formulation is given by [55]:

$$f_a \frac{\epsilon_a - \epsilon}{\epsilon_a - 2\epsilon} + (1 - f_a) \frac{\epsilon_b - \epsilon}{\epsilon_b - 2\epsilon} = 0 \quad (10)$$

where  $\epsilon_a$  and  $\epsilon_b$  are the dielectric constants of components a and b, respectively. The  $f$  and  $1 - f_a$  denote the volume fractions of components a and b, respectively. The real part of optical conductivity ( $\sigma_1$ ) is related to the imaginary part

of the dielectric constant ( $\epsilon_2$ ) through the following equation [55]:

$$\sigma_1(\omega) = \frac{\omega \epsilon_2}{4\pi}. \quad (11)$$

Meanwhile, the absorption coefficient, which is associated with the imaginary refractive index, can be calculated as follows [62].

$$\alpha = \frac{4\pi k}{\lambda}. \quad (12)$$

## 2.6 SPR characteristics measurements

SPR characteristics were measured using the Kretschmann configuration with the sample structures of  $S_1$ ,  $S_2$ ,  $S_3$ ,  $S_4$ ,

and  $S_5$ , as described in the ellipsometry tests. The setup of the SPR homemade components is displayed in Fig. 5 and has been reported in detail in previous studies [63]. The mechanism of an electric field application to the sample's surface is the same as that performed in the ellipsometry test. A voltmeter was used during the measurement process to monitor voltage variations at 30-second intervals during the 7-minute observation period (representing one SPR measurement cycle).

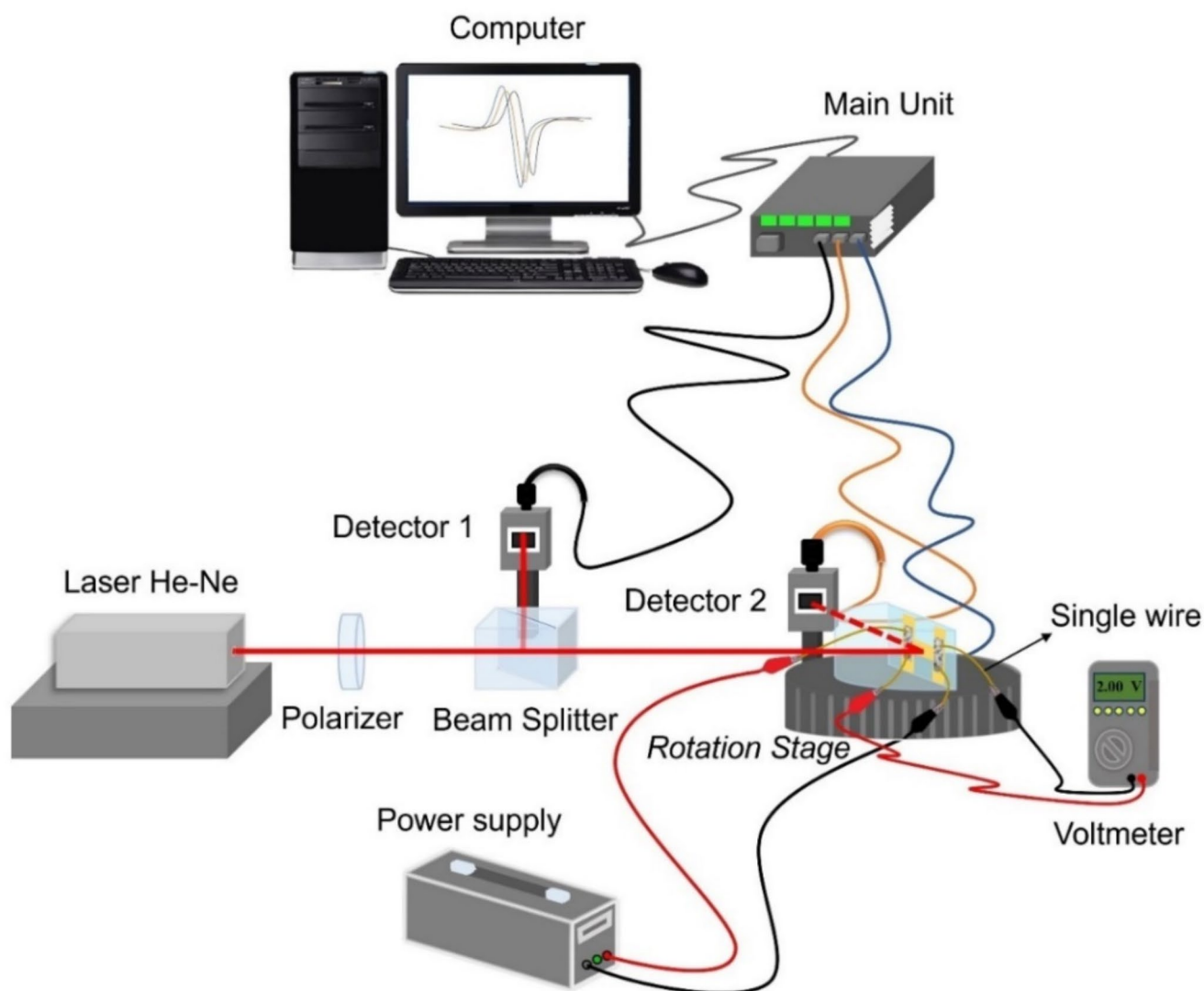


**Fig. 5** Setup of SPR Spectroscopy under an electric field. The voltage from the power supply is induced to the Au surface using a single wire, while a voltmeter reads the incoming voltage on the Au thin film

### 3 Result and discussion

#### 3.1 Phase, morphology, magnetic properties, and composition of magnetite/silver NCs

The successful combination of magnetite and silver was characterized by the presence of magnetite NPs diffraction peaks at 220, 311, 400, 511 and 440 and silver NPs at 111 and 220, as shown in Fig. 6(a). The lattice parameters of magnetite and silver are 0.81 and 0.41, respectively, and the phase composition is 91.5 and 8.5, respectively. Magnetite

and magnetite/silver lattice parameters are 13.7 and 12.7, respectively. The magnetite NPs and magnetite/silver NCs exhibit soft ferromagnetic with the saturation magnetization ( $M_s$ ) at about 77 emu/g and 52 emu/g, respectively, the magnetic remanence ( $M_r$ ) is 8 and 12.7 emu/g, and the coercive field is 49 and 156 Oe, respectively, as shown in Fig. 6(b). Meanwhile, the NCs are mostly spherical, with an average size of  $13.22 \pm 0.78$  nm, as shown in Fig. 6(c). Meanwhile, three distinctive elements are observed in the NCs with the composition of Fe 55%, O 24%, and Ag 20%, indicating

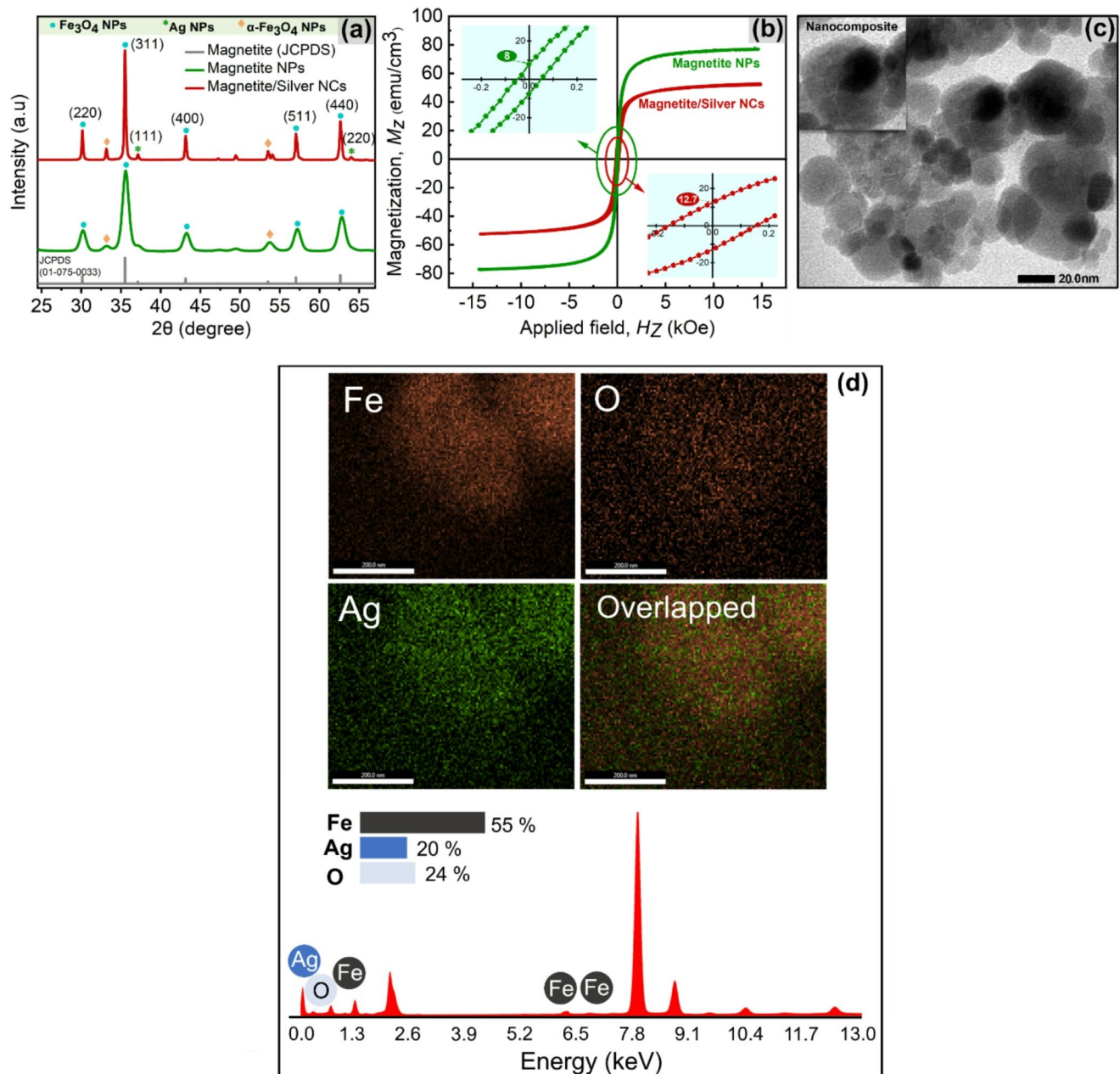


**Fig. 6** (a) The image of the XRD spectrum, (b) FTIR curve, (c) TEM image, and (d) Elemental mapping with the EDX spectrum of the NCs. (Modified from Riswan et al. [46] under CC BY-NC-ND license).

the successful deposition of silver NPs on the surface of the magnetite NPs, as depicted in Fig. 6 (d).

### 3.2 Optical properties studies

Figure 7 featured the experimental parameters of  $\psi$  and  $\Delta$  of the 40 nm air/EMA/Au film/glass observed at a  $75^\circ$  incident angle. The amplitude ratio ( $\psi$ ) value denotes the refractive index,  $n$ , while the phase difference ( $\Delta$ ) value denotes the extinction coefficient,  $k$ , of the material. The value of  $\psi$  does not change too much with the angle of incidence because the reflected p-polarized and s-polarized light is almost equal in magnitude. Meanwhile, the angle-of-incidence dependent  $\Delta$  value lowers as the electric field amplitude increases, implying a change in the optical parameter. The outcomes of the model fitting demonstrate promising performance, as evidenced by an overall mean square error (MSE or  $\chi^2$ ) of 0.05,

below 1, indicating a perfect fitting result. The figure shows the  $\psi$  and  $\Delta$  of Au thin film and magnetite/silver NCs with and without an electric field application.

We now present the optical properties of the sample structure of a glass substrate/Au film and a glass substrate/Au film/ magnetite/silver NCs with varied electric fields in the photon energy of 1.5–5 eV. Applying an electric field leads to improved optical properties of NCs, as seen in Fig. 8. The  $\text{Fe}_3\text{O}_4$  and Ag NPs absorb incident photons, which excite electrons in the valence band, causing them to move to the conductive band of Ag. When  $\text{Fe}_3\text{O}_4$  and Ag NPs form a composite structure, free electrons migrate from the Fermi level of  $\text{Fe}_3\text{O}_4$  to the conductive band of Ag, achieving an equilibrium Fermi state. Applying an electric field increases the number of charge carriers, affecting the electron transition and changing the equilibrium Fermi state, thereby improving the NC's optical properties [64]. The real part

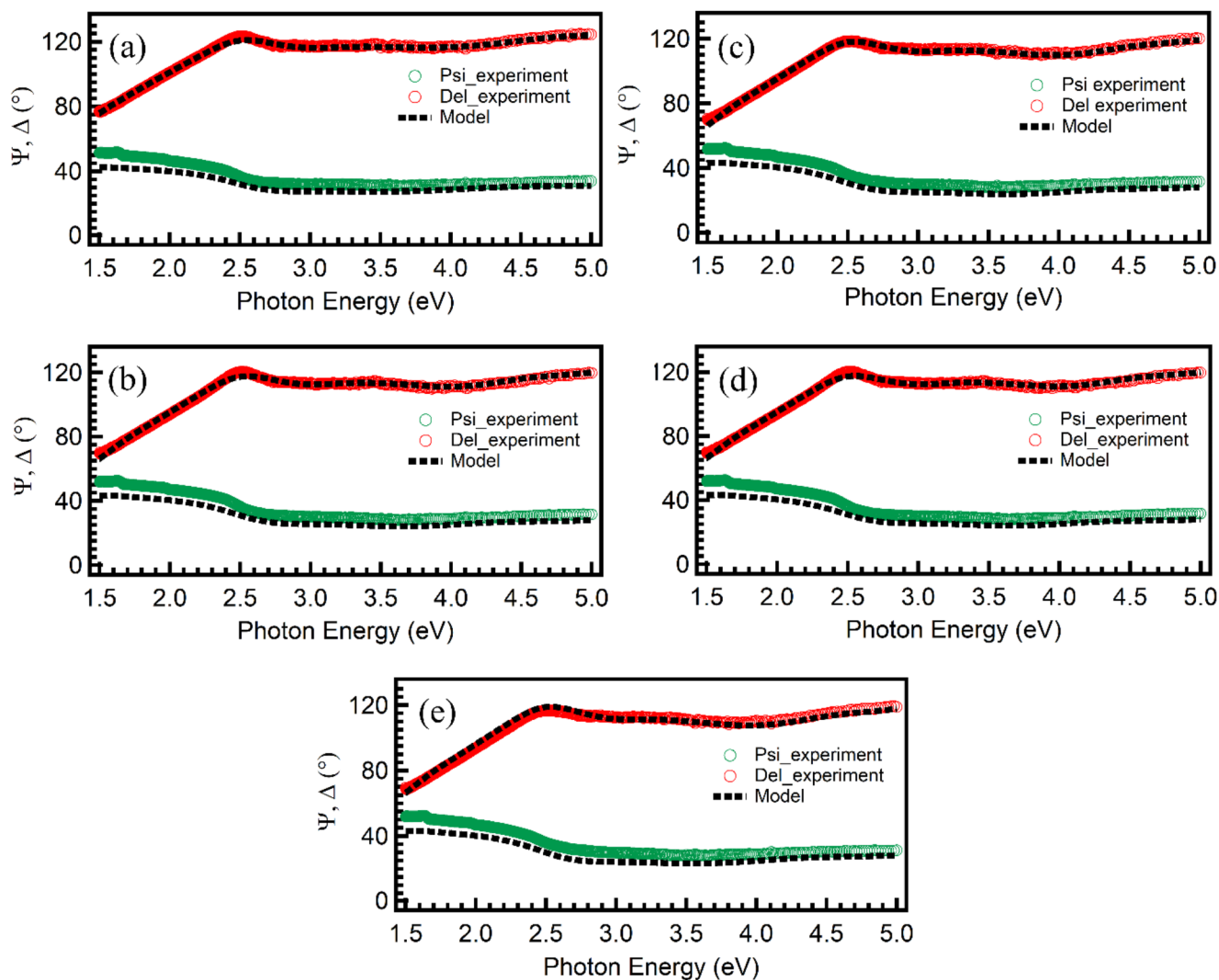


**Fig. 7** The  $\psi$  and  $\Delta$ , observed at an incidence angle of  $75^\circ$ . (a) Au thin film, (b) magnetite/silver NCs, (c) magnetite/silver NCs,  $E=1.6$  V/cm, (d) magnetite/silver NCs,  $E=2.4$  V/cm, (e) magnetite/silver NCs,

$E=3.2$  V/cm. The red, green, and dashed lines are the  $\psi$  experiment,  $\Delta$  experiment, and model, respectively

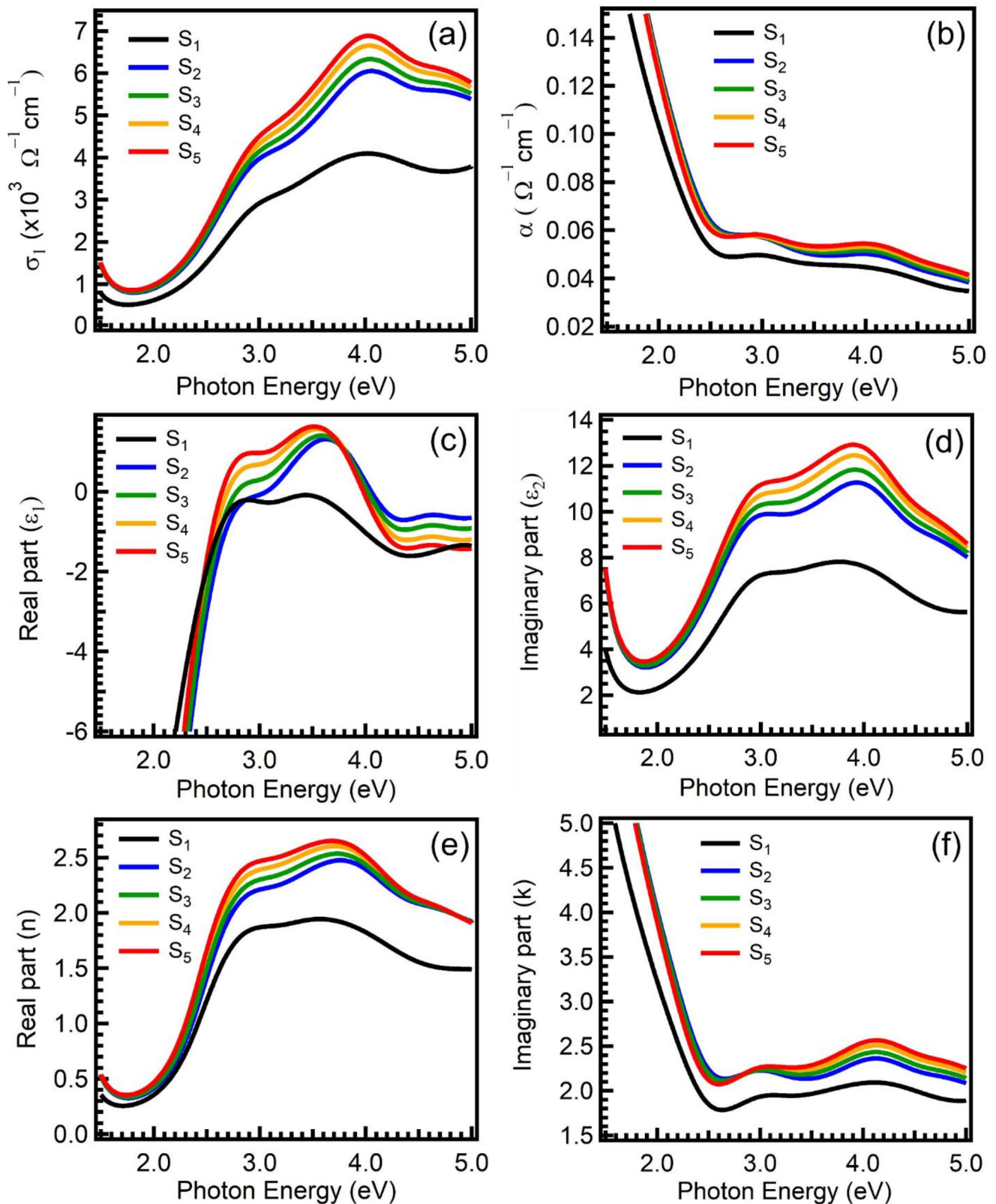


**Fig. 8** (a) the real part ( $\sigma_1$ ) of optical conductivity, (b) the optical absorption ( $\alpha$ ), (c) and (d) is the real part ( $\epsilon_1$ ), and the real imaginary ( $\epsilon_2$ ) of dielectric constant, and (e) and (f) are the real part ( $n$ ) and the imaginary part ( $k$ ) of the refractive index. The black line is for the

structure of the glass substrate/Au film. Blue, green, orange, and red lines for the structure of glass substrate/Au film/magnetite/silver NCs without electric field, with electric field of 1.6 V/cm, 2.4 V/cm, and 3.2 V/cm, respectively

of optical conductivity ( $\sigma_1$ ) and optical absorption ( $\alpha$ ) are shown in Fig. 8a and b. The deposition of the NCs on the surface of an Au film causes an increase in the  $\sigma_1$  in all photon energy, a significant increase occurred in the high energy range of 3–5 eV. In the high photon energy of 3–5 eV, the application of an electric field causes the same trend of increasing  $\sigma_1$ , the greater the applied electric field, the more significant the increase in  $\sigma_1$ . However,  $\sigma_1$  is almost constant for low energy of 1.5–3 eV. This might occur because at low energies, the electric field is not strong enough to affect the electrons and change the  $\sigma_1$  of the material. The addition of the NCs increases the  $\alpha$  in all photon energy ranges.  $\alpha$  indicates the absorption ability of the NCs, where the increase in  $\alpha$  is relatively tiny but non-negligible at the high energy of 3–5 eV after the applied electric field and remains relatively constant in the low energy range. The variation in  $\epsilon_1$  increase after the addition of the NCs in the high photon energy, as shown in Fig. 8c. Applying an electric field increases in  $\epsilon_1$  in the low photon energy of 2.2 eV–3.5 eV, and a decrease in  $\epsilon_1$  occurs at high energy for electric field variation.  $\epsilon_1$  is related to the polarization curvature caused by the electric field of electromagnetic waves. In the energy range of 3.5–5 eV, a switching trend occurs, where the increase in the electric field causes a decrease in  $\epsilon_1$ . In addition, in the range of 2.5 to 4 eV, the application of the electric field causes a change in plasmonic characteristics to non-plasmonic, which is characterized by a positive  $\epsilon_1$  value, indicating no surface resonance in that energy range [64, 65]. These variations in  $\epsilon_2$  reflect to those in  $\sigma_1$  through Eq. (11), where the variation becomes significant at the higher energy level, as shown in Fig. 8d. Meanwhile, Fig. 8e and f show the variation in  $n$  and  $k$ , where the trend in  $n$  follows by that in  $\epsilon_2$ , and the variation in  $k$  reflects those of  $\alpha$  through Eq. (12), where the variation increases relatively small but non-negligible at the high energy.

### 3.3 SPR properties studies

#### 3.3.1 LSPR behavior studies

We now investigate the influence of the NCs deposition on the SPR curve characteristics by varying the incident light wavelengths of 405, 450, and 632.8 nm. Figure 9 shows that NCs deposition causes a higher SPR angle and minimum reflectance for three-wavelengths. The increase in SPR angle after NCs deposition is 1.21, 0.97, and 0.66 for wavelengths 405, 450, and 632.8 nm, respectively. The shift of SPR angle after the deposition of the NCs on the surface of the Au film is caused by the change in the surface plasmon wavevector, leading to a modification in the resonance condition. The resonance condition between evanescent wave

and surface plasmon wave occurs when the following condition is satisfied [10]:

$$k_{EW} = k_{SPW}. \quad (13)$$

Where the wavevector of the evanescent wave propagating along the prism/metal interface is formulated as follows [38, 66]

$$k_{EW} = \frac{2\pi}{\lambda} \sqrt{\epsilon_p} \sin(\theta_0) \quad (14)$$

where  $\lambda$  is a wavelength of the incident light,  $\epsilon_p$  is a dielectric function of the prism, and  $\theta_0$  is an incident angle. The surface plasmon wave (SPW) wavevector along the metal/dielectric interface is [20].

$$k_{SPW} = \frac{\omega}{c} \sqrt{\frac{\epsilon_m \epsilon_d}{\epsilon_m + \epsilon_d}} \quad (15)$$

where  $\omega$  represents the angular frequency of the wave,  $c$  denotes the speed of light in a vacuum,  $\epsilon_m$  and  $\epsilon_d$  are dielectric functions of the metals and dielectric, respectively

The deposition of magnetite/silver NCs into the prism/Au film system modifies the material's dielectric function to a combined material dielectric function, as shown in Eq. 14, leading to a change in the wavevector of the surface plasmon wave, which in turn adjusts the resonance condition and induces a shift in the SPR angle. The deposition of the NCs results in an enhanced electric field of electromagnetic waves around the NCs, a phenomenon known as LSPR. The interaction between photons and free electrons on the surface of the Au film and nanoparticles causes a robust coupling between surface plasmons localized around the nanoparticles and surface plasmons propagating on the surface of the Au film [45]. LSPR occurs due to the confinement of surface plasmons inside NCs whose size dimensions are comparable to or smaller than the wavelength of the incident light. When incident light hits the metal nanoparticles, the electric field oscillates coherently with the conduction electrons, resulting in a Coulomb attraction between the electrons and the nucleus that causes the electron cloud to shift from equilibrium. As a result, a restoring force is generated, causing the electron cloud to oscillate. The frequency of these oscillations is governed by factors such as effective electron mass, electron density, and the size and morphology of the charge distribution.

In the LSPR phenomenon, plasmons undergo local oscillations on the NCs, which leads to a shorter electromagnetic field decay length than SPR and thus increases the sensitivity to changes in the refractive index of the NCs surface. In addition, LSPR shows two significant effects: first, the

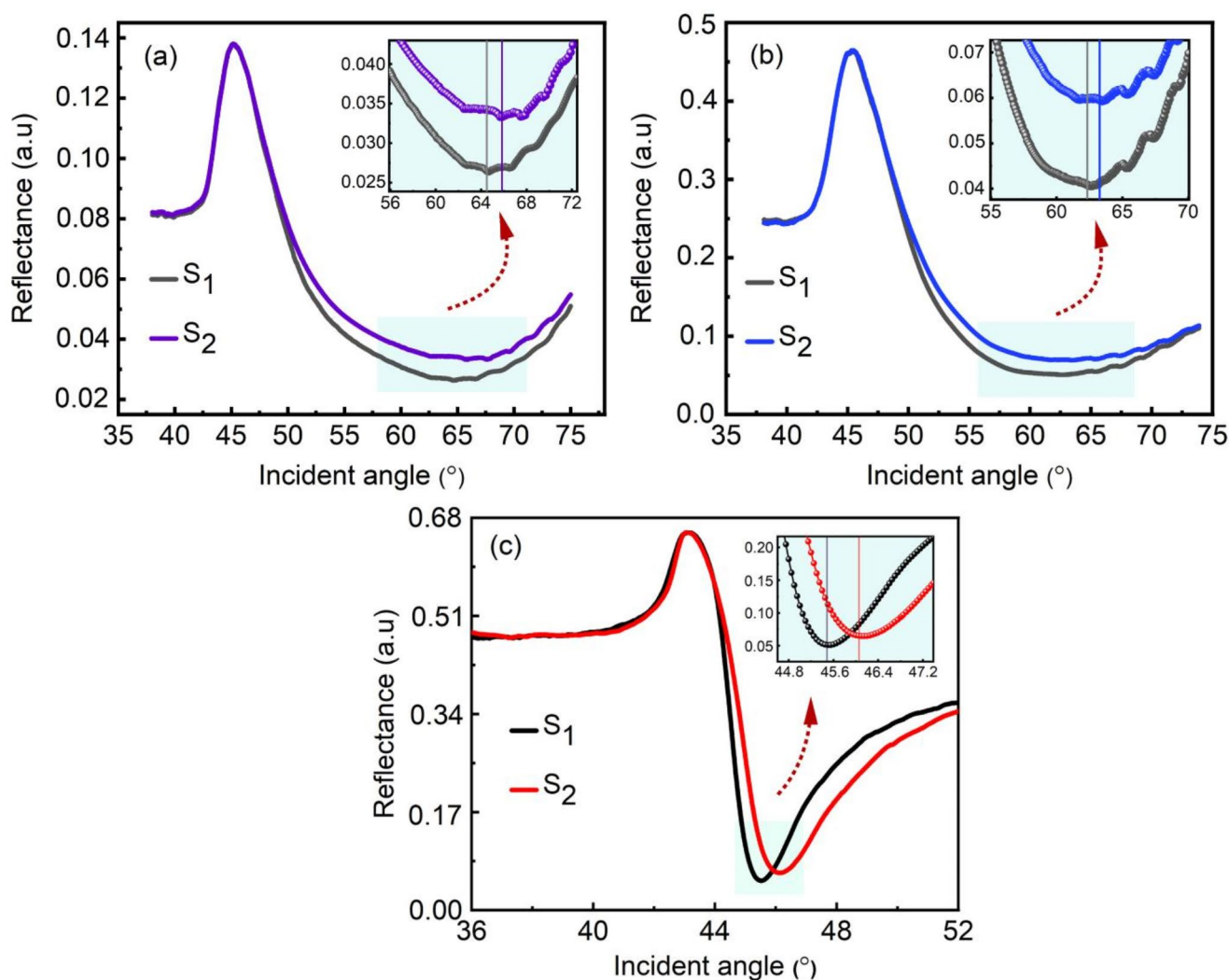


**Fig. 9** SPR curves of a prism/Au film marked by black line, and a prism/Au film/magnetite/silver NCs/air system, marked by purple, blue, and red line, with light source wavelength of (a) 405 nm, (b) 450 nm, and (c) 632.8 nm

electric field near the NCs surface undergoes a substantial increase, peaking at the surface and decaying rapidly with distance; second, the optical extinction of NCs shows a maximum at the plasma resonance frequency, which typically occurs in the wavelength range seen for noble metal nanoparticle. Meanwhile, the addition of the conjugated mass of the NCs causes a change in the refractive index, which modifies the intersection point between the evanescent and surface plasmons on the dispersion relation curve. The dielectric constant of a composite material is the result of a combination of the dielectric constants of each constituent material. Composite structures exhibit different optical properties due to the interaction between two materials with different optical characteristics, which significantly improves the overall optical behaviour.

In addition, the variation in the SPR angle after the wavelength of incident light is varied is caused by the

modification in the evanescent wavevector, as pointed out in Eq. 13. The wavevector of the evanescent wave is inversely proportional to the wavelength of the incident light. A decrease in the wavelength of the light source leads to an increase in the wavevector of the evanescent wave, causing a higher resonance condition, characterized by a higher LSPR angle, as described in Eq. 12. Meanwhile, the LSPR curve profiles of 405 (Fig. 9a) and 450 nm (Fig. 9b), are broader than at 632.8 nm (Fig. 9c), a possible explanation for this is that electrons undergo oscillation damping at the metal/dielectric interface, leading to higher losses in the surface plasmon polariton mode as the curve broadens. As a result, the LSPR feature becomes less pronounced and more challenging to observe. In contrast, the peak excitation of surface plasmon waves occurs at a wavelength of 632.8 nm, as evidenced by a sharp, deep curve and a notable shift in the LSPR angle.

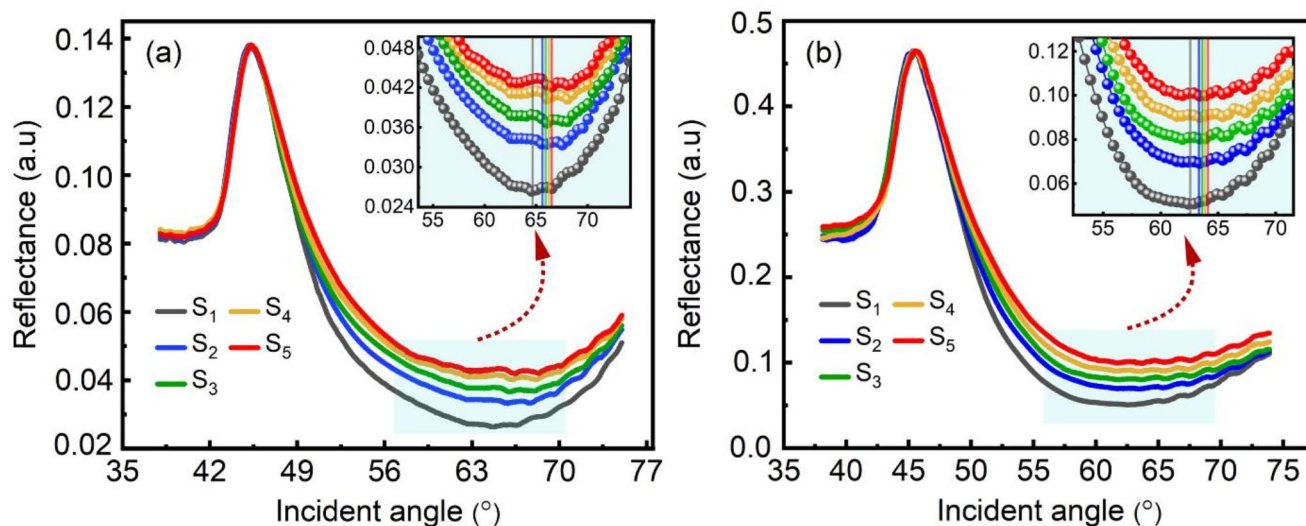


**Fig. 10** SPR curves of a prism/Au film/magnetite/silver NCs/air system under an electric field with light source wavelength of (a) 405 nm and (b) 450 nm. Colour notations are the same as Fig. 8

**Table 2** SPR angles of the sample for a Prism/Au film/magnetite/silver NCs/air under an electric field (405 nm)

Sample system	Applied electric field	SPR angles (°)	SPR angles shift (°)
Au thin film	-	64.62	0
Au/magnetite/silver NCs	-	65.87	1.25
Au/magnetite/silver NCs	1.6 V/cm	65.99	1.37
Au/magnetite/silver NCs	2.4 V/cm	66.23	1.61
Au/magnetite/silver NCs	3.2 V/cm	66.49	1.87

**Table 3** SPR angles of the sample for a Prism/Au film/magnetite/silver NCs/air under an electric field (450 nm)

Sample system	Applied electric field	SPR angles (°)	SPR angles shift (°)
Au thin film	-	62.60	-
Au/magnetite/silver NCs	-	63.41	0.81
Au/magnetite/silver NCs	1.6 V/cm	63.62	1.02
Au/magnetite/silver NCs	2.4 V/cm	63.77	1.20
Au/magnetite/silver NCs	3.2 V/cm	63.94	1.32

### 3.3.2 LSPR-based electro optic studies

This section investigates the impact of the electric field on the LSPR of magnetite/silver NCs using wavelengths of 405, 450, and 632 nm. Figure 10a shows the SPR curve characteristic of the NCs with a wavelength of 405 nm. After applying the electric field, the LSPR angle shifted from 65.87° to 65.99°, 66.23°, and 66.49° for the electric field of 1.6, 2.4, and 3.2 V/cm, respectively. Meanwhile, Fig. 10b shows the SPR curve characteristic with a wavelength of 450 nm. After applying the electric field, the LSPR angle

shifted from 63.41° to 63.62°, 63.77°, and 63.94° for electric fields of 1.6, 2.4, and 3.2 V/cm, respectively. In addition, the minimum reflectance increases quite significantly with the increase in the electric field amplitude, as shown in detail in Tables 2 and 3, verified that the light reflected at resonant conditions can be tuned through the applied electric field.

Applying an electric field to LSPR modulates the surface plasmon's optical properties, signal intensity, and resonant frequency. This modulation occurs by strengthening the local electric field around the NCs when an electric field is applied. The applied electric field causes the polarization of free electrons in the metal nanoparticles, which alters the direction and strength of the local electric field generated by the LSPR resonance; as a result, the resonance position between the evanescent wave and the surface plasmon wave, leading to an increase in LSPR sensitivity. The optical properties of the material highly depend on the magnitude of an electric field. As depicted in Fig. 10, a stronger electric field leads to a more substantial change in the LSPR angle, as shown in Tables 2 and 3.

Figure 11 demonstrates the LSPR excitation phenomenon after applying an electric field. The electric field of an electromagnetic wave interacts with the surface charge on the nanoparticles, strengthening the nanoparticle surface electric field. When an external electric field is applied, this surface electric field will be further amplified due to the polarization of the surface charge, which leads to the accumulation of additional charge that amplifies the surface electric field of the sensor, resulting in a modified LSPR signal. Furthermore, the polarization induced by the electric field can cause modification in the dielectric tensor of the material. The dielectric tensor is a measure that characterizes how a material responds to an electric field. The

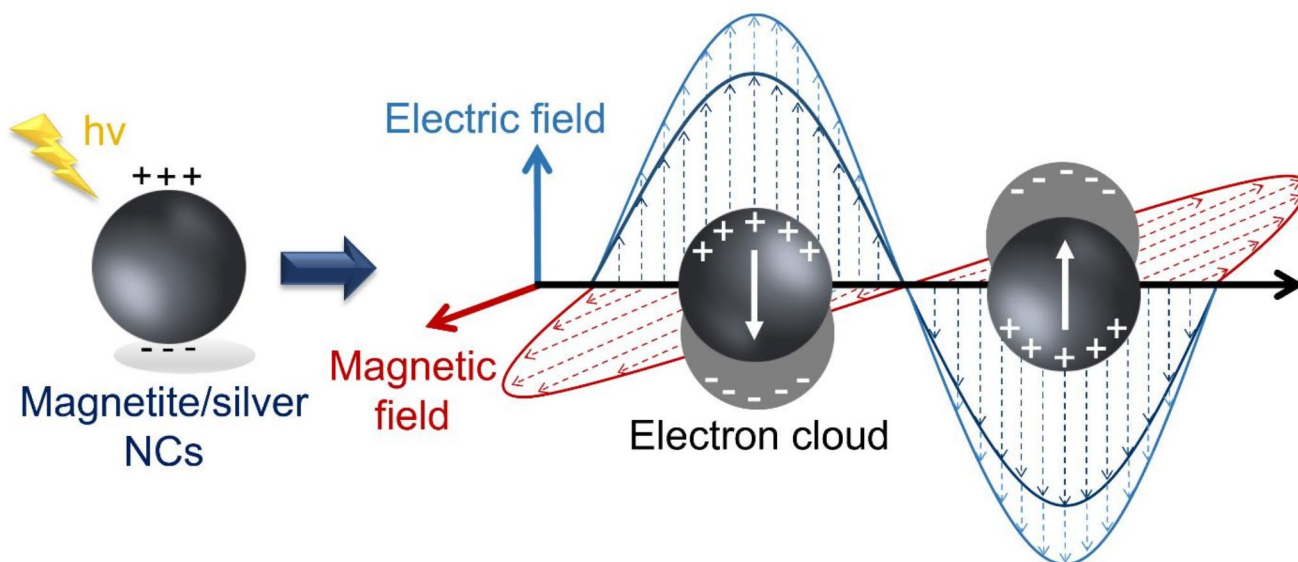


**Fig. 11** Schematic diagram of LSPR after applying an electric field. Red and blue wavy lines are the magnetic and electric fields of the electromagnetic wave, respectively. The light blue line shows an increase in the electric field after the induced electric field

alteration in the dielectric tensor of a material caused by the perturbation caused by an electric field is described by the following equation [50]:

$$\overleftrightarrow{\epsilon}' = \overleftrightarrow{\epsilon} + \overleftrightarrow{\Delta\epsilon}, \tag{16}$$

where  $\overleftrightarrow{\epsilon}'$  denotes modification of the dielectric tensor due to the electric field effect,  $\overleftrightarrow{\epsilon}$  signifies the initial dielectric tensor before the contribution of the electric field, and  $\overleftrightarrow{\Delta\epsilon}$  represents the perturbed dielectric tensor.

The change in the dielectric tensor due to the application of an electric field can be described by a perturbed dielectric tensor, which characterizes the sensor surface's response to the external electric field [67]. Without an electric field, the molecular orientation on the sensor surface is defined by the dielectric tensor in its unperturbed state (zero-dielectric tensor). However, upon the application of an electric field to the sensor surface, a perturbed dielectric tensor is created, which can be represented as follows [68]:

$$\overleftrightarrow{\Delta\epsilon} = i\epsilon \begin{bmatrix} 0 & -\eta P_z & \eta P_y \\ \eta P_z & 0 & -\eta P_x \\ -\eta P_y & \eta P_x & 0 \end{bmatrix} \tag{17}$$

In this context,  $P_x$ ,  $P_y$ , and  $P_z$  denote the polarization component of the material, while  $\eta$  denotes the electrical impermeability, expressed as  $\eta = \epsilon_0/\epsilon = 1/n^2$ . In electro-optical phenomena, when an electric field is induced to the SPR, the electrical impermeability may be altered through changes in the refractive index of the sensor surface.

Modifying the dielectric tensor of the material after applying an external electric field causes a modification in

the SPW wave vector, thus modifying the dispersion relation and changing the SPR angle [69].

$$\theta_{SPR} = \sin^{-1} \left( \sqrt{\frac{1}{\epsilon_{pr}} \frac{\epsilon_m \epsilon_a}{\epsilon_m + \epsilon_a}} \right) \tag{18}$$

In addition, the applied electric field also has an impact on the SPR reflectance, as shown in Fig. 10. Alterations in the optical properties of materials resulting from the application of electric fields also result in changes in the amplitude of the reflection coefficient of light. In the Kretschmann configuration, the SPR can be visualized as a dip in the reflectance curve at a particular angle of incidence. To obtain the reflectance of the light, we employed the transfer matrix method. For p-polarised light, the Fresnel reflection coefficients for layered media are given by [70]:

$$r_{jk} = \frac{k_{zj}/\epsilon_j - k_{zk}/\epsilon_k}{k_{zj}/\epsilon_j + k_{zk}/\epsilon_k} \tag{19}$$

Where  $r_{jk}$  is the reflection coefficient for the  $j$ - $k$  interface,  $\epsilon_j$  and  $\epsilon_k$  are the electric permittivities of  $j^{th}$  and the adjacent  $k^{th}$  media, respectively. The  $k_{zj}$  and  $k_{zk}$  are propagation constants of  $j^{th}$  and  $k^{th}$  media that are given by [71]:

$$k_{zj} = k_0 \sqrt{\epsilon_j - \epsilon_1 \sin^2 \theta} \tag{20}$$

$$k_{zk} = k_0 \sqrt{\epsilon_k - \epsilon_1 \sin^2 \theta} \tag{21}$$

Where  $\epsilon_1$  is the electric permittivity of the prism. Thus, the reflectance for a four-layer system ( $R_{1234}$ ) [prism (1) - Au thin film (2) - NPs (3) - air (4)] can be calculated using equations as [70]

$$(R_{1234}) = \left| \frac{r_{12} + r_{23} e^{i2k_z d_2} + r_{34} e^{i2k_z d_2} e^{i2k_z d_3} + r_{12} r_{23} r_{34} e^{i2k_z d_3}}{1 + r_{12} r_{23} e^{i2k_z d_2} + r_{23} r_{34} e^{i2k_z d_3} + r_{12} r_{34} e^{i2k_z d_3}} \right|^2 \quad (22)$$

Here,  $r_{12}$ ,  $r_{23}$ , and  $r_{34}$  are the Fresnel coefficient of reflections at the interfaces of prism-Au thin film, Au film-NCs, and NCs-air, respectively.  $k_{z2}$ ,  $k_{z3}$ ,  $d_2$  and  $d_3$  are propagation constants of light in Au thin film and NCs, the thickness of Au thin film and thickness of analyte layer, respectively (shown in Fig. 3).  $k_{z1}$  and  $k_{z4}$  are the propagation constants of light in prism and air, respectively.

The utilization of the electric field increases the SPR performance characterized by the increase in SPR angle and minimum reflectance. By controlling the magnitude of the electric field applied to the LSPR, the sensitivity and selectivity of the LSPR can be adjusted. An electric field can be used to control the depth of penetration of the evanescent field into the detected sample, affecting the resolution and sensitivity of the SPR sensor. In addition, the application of an electric field causes changes in charge density, NCs orientation, and surface electron distribution on the sensor's surface, modifying the dielectric constant and changing the LSPR properties of the NCs. Applying an electric field modifies the phase-coupling conditions and allows for changes in the characteristics of electro optic-based SPR.

Some findings have been reported to investigate the electric field effect on the LSPR biosensor, such as the study performed by Ju-Won Jeon et al. 2016 who found that applying electric potential from  $-0.3$ ,  $0.5$  V with the increment of  $0.1$  to Au nanocubes (NCs)/@ polyaniline (PANI) core/shell nanostructure, with  $0.5$  M NaCl in  $0.01$  M HCl electrolyte causes the position of the UV-vis absorption peak to shift to the left as the LSPR peak shifts from  $555$  to  $533$  nm (blue shift). The change is due to the change in refractive index. Meanwhile, in the case of the non-aqueous electrolyte,  $0.5$  M lithium bis(trifluoromethyl)sulfonylimide (LiBTI) in propylene carbonate (PC), a smaller LSPR shift (up  $17$  nm) was obtained with a  $26$  nm PANI shell. At high positive potentials above  $0.2$  V, the LSPR peak shifted red when the applied voltage increased from  $0.2$  V to  $0.4$  V [72]. Another study conducted by Petr A. Ledin et al. 2015 applied an electric field from  $-0.2$  to  $0.5$  V in an increasing manner with the increment of  $0.1$  on the sample structure of Au nanorods/ITO in LiBTI/acetone nitrile as an electrolyte resulting in a  $3$  nm red shift of the longitudinal mode with a slight decrease of LSPR intensity [73]. A similar result was reported by Gupta et al. [74], they used the structure of a prism/air gap/SBN60/LSCO/Si thin-film multi-structure to

**Table 4** Comparison of electro-optic-based LSPR research results

Sample structure	Voltage	Experiment result	Ref.
Glass/ITO/Au film/Au NPs	$-900$ to $+900$ mV	A positive voltage causes a redshift of the LSPR peak from $569$ to $591$ nm, while a negative voltage induces a blue shift.	[75]
LiNbO <sub>3</sub> /Au film/HSA-coated Au NPs/analyte solution	$-1$ , $-0.5$ , $0$ , $0.5$ , and $1$ V	The power ratio increases linearly with the voltage	[76]
Au NPs/Lead zirconate titanate (PZT)	$50$ , $250$ , and $500$ kV/cm	Applied electric fields cause the SPR signals to red-shifted to $618$ , $625$ , and $649$ nm, respectively	[77]
Glass/Au nanohole arrays	$-600$ , $-450$ , $-300$ , $-150$ , $150$ , $300$ , $450$ , and $600$ mV	The SPR spectrum at $1$ $\mu$ g/mL CRP concentration shifts linearly with the applied DC voltage.	[78]
Prism/Au/Magnetite/Silver NCs	$0$ , $2$ , $3$ , and $4$ V	The LSPR angle shifts from $65.87$ to $65.99$ , $66.23$ , and $66.49$ for $405$ nm wavelength and shifts from $63.41$ to $63.62$ , $63.77$ , and $63.94$ for $450$ nm wavelength.	This study

investigate waveguide-coupled surface plasmon resonance-based electro-optic modulation by applying electric field from  $25$  to  $200$  kV/cm. They found that a continuous shift towards higher angles is seen in reflectance spectra for the WCSPR-SBN75 EO modulator system with increasing the amplitude of the applied DC electric field. A continuous shift in SPR reflectance angle ( $\theta_{SPR}$ ) from  $49.93$  to  $50.92$  was observed owing to subsequent change in refractive index of SBN75 layer with different applied field amplitude varying from  $0$  kV/cm to  $200$  kV/cm. They observed a continuous shift to higher angles in the reflectance spectra of the WCSPR-SBN75 EO modulator system as the amplitude of the applied DC electric field increased. The SPR reflectance angle ( $\theta_{SPR}$ ) shifted continuously from  $49.93^\circ$  to  $50.92^\circ$ , which was attributed to the change in the refractive index of the SBN75 layer as the applied field amplitude varied from  $0$  kV/cm to  $200$  kV/cm. The variation in the refractive index of the SBN75 thin film also leads to an increase in the fitted minimum reflectance ( $R_{min}$ ) value, rising from  $0.807$  to  $0.881$  as the electric field amplitude increases. Comparison of LSPR research results with the application of electric fields can be seen in more detail in Table 4. The results reported in previous research are directly proportional to this study, where a higher applied electric field leads to a redshift in the LSPR angle (the LSPR angle increases). The change in SPR characteristics through the application of an electric field indicates that the electro-optic effect affects the optical properties of the material. As the electric field increases, the

alteration in the material's optical properties becomes more significant, resulting in a greater change in the LSPR angle and minimum reflectance. Therefore, the application of an electric field to LSPR sensors offers excellent potential for enhancing the selectivity and sensitivity of SPR biosensors and developing electronically controlled optical devices.

## 4 Conclusion

The study of optical properties and localized surface plasmon resonance (LSPR) of magnetite/silver NCs has been successfully investigated. The NCs were synthesized using the co-precipitation method and coated on the Au film surface with a four-layer Kretschmann configuration system. Light source wavelengths of 405 and 450 nm were used to investigate the influence of the varied wavelength on the optical properties and LSPR curve characteristics. Electric fields of 1.6, 2.4, and 3.2 V/cm were applied to the substrate/Au film/magnetite/silver NCs/air sample structure for ellipsometer and SPR testing. The findings indicate that the use of an electric field improves the optical properties, a real part of optical conductivity  $\sigma_1$ , complex dielectric constant (real part,  $\epsilon_1$  and imaginary part,  $\epsilon_2$ ), complex refractive index (real part,  $n$  and imaginary part,  $k$ ), and optical absorption ( $\alpha$ ), resulting in a rise in the LSPR angle and a decrease in minimum reflectance. Furthermore, the variation in the incident light wavelength at 405, 450, and 632.8 nm causes an increase in the LSPR angle by 1.21, 0.97, and 0.66, respectively. At a wavelength of 405 nm, the application of electric fields of 1.6, 2.4, and 3.2 V/cm induced shifts in the LSPR angle from 65.87° to 65.99°, 66.23°, and 66.49°, respectively. At 450 nm, the LSPR angle shifted from 63.41° to 63.62°, 63.77°, and 63.94°, respectively. The significant change in the LSPR angle and minimum reflectance due to the applied electric field and wavelength indicates that the application of an electric field to LSPR sensor surface with varied wavelengths provides the scenario to improve the performance of SPR biosensors for future applications.

**Supplementary Information** The online version contains supplementary material available at <https://doi.org/10.1007/s42247-025-01085-w>.

**Acknowledgements** The authors would like to thank for the scholarship of PMDSU 2022–2024, the Ministry of Education, Culture, Research & Technology (Republic of Indonesia).

**Author contributions** Muhammad Riswan: conceptualization, methodology, investigation, validation, formal analysis, writing – original draft preparation. Eri Widiyanto: investigation, validation, formal analysis. Hervin Maulina: investigation, validation, formal analysis. Muhammad Arifin: conceptualization, methodology. Iman Santoso: conceptualization, methodology, validation, supervision, writing – review & editing. Edi Suharyadi: Conceptualization, validation, fund-

ing acquisition, project administration, supervision, writing – review & editing.

**Data availability** The data supporting this study's findings are available on request from the corresponding author.

## Declarations

**Conflict of interest** No conflict of interest.

## References

1. K. Yeneayehu, T. Senbeta, B. Mesfin, Enhancement of the optical response of Fe<sub>3</sub>O<sub>4</sub>@Ag core-shell nanoparticles. *Phys. E Low-Dimensional Syst. Nanostruct.* **134**, 114822 (2021). <https://doi.org/10.1016/j.physe.2021.114822>
2. S.K. Ghosh, T. Pal, Interparticle coupling effect on the surface plasmon resonance of gold nanoparticles: from theory to applications. *Chem. Rev.* **107**, 4797–4862 (2007). <https://doi.org/10.1021/cr0680282>
3. J. Pérez-Juste, P. Mulvaney, L.M. Liz-Marzán, Patterning and encryption using gold nanoparticles. *Int. J. Nanotechnol.* **4**, 215–225 (2007). <https://doi.org/10.1504/IJNT.2007.013468>
4. A. Akbarzadeh, D. Zare, A. Farhangi, M.R. Mehrabi, D. Norouziyan, S. Tangestaninejad, M. Moghadam, N. Bararpour, Synthesis and characterization of gold nanoparticles by Tryptophane. *Am. J. Appl. Sci.* **6**, 691–695 (2009). <https://doi.org/10.3844/ajas.2009.691.695>
5. W. Brullot, V.K. Valev, T. Verbiest, Magnetic-plasmonic nanoparticles for the life sciences: calculated optical properties of hybrid structures, nanomedicine nanotechnology. *Biol. Med.* **8**, 559–568 (2012). <https://doi.org/10.1016/j.nano.2011.09.004>
6. S. Swami, F. Kayenat, S. Wajid, SPR biosensing: cancer diagnosis and biomarkers quantification. *Microchem J.* **197**, 109792 (2024). <https://doi.org/10.1016/j.microc.2023.109792>
7. X. Huang, M.A. El-Sayed, Plasmonic photo-thermal therapy (PPTT). *Alexandria J. Med.* **47**, 1–9 (2011). <https://doi.org/10.1016/j.ajme.2011.01.001>
8. G.I. Janith, H.S. Herath, N. Hendeniya, D. Attygalle, D.A.S. Amarasinghe, V. Logeeshan, P.M.T.B. Wickramasinghe, Y.S. Wijayasinghe, Advances in surface plasmon resonance biosensors for medical diagnostics: an overview of recent developments and techniques. *J. Pharm. Biomed. Anal. Open.* **2**, 100019 (2023). <https://doi.org/10.1016/j.jpba.2023.100019>
9. H.H. Nguyen, J. Park, S. Kang, M. Kim, Surface plasmon resonance: A versatile technique for biosensor applications. *Sens. (Switzerland)*. **15**, 10481–10510 (2015). <https://doi.org/10.3390/s150510481>
10. N. Adrianto, A.M. Panre, N.I. Istiqomah, M. Riswan, F. Apriliani, E. Suharyadi, Localized surface plasmon resonance properties of green synthesized silver nanoparticles. *Nano-Structures Nano-Objects.* **31**, 100895 (2022). <https://doi.org/10.1016/j.nanoso.2022.100895>
11. Y. Yanase, T. Hiragun, K. Ishii, T. Kawaguchi, T. Yanase, M. Kawai, K. Sakamoto, M. Hide, Surface plasmon resonance for cell-based clinical diagnosis. *Sensors.* **14**, 4948–4959 (2014). <https://doi.org/10.3390/s140304948>
12. S. Balbinot, A. Mohan, J. Vidic, I. Abdulhalim, M. Manzano, Trends in food science & technology plasmonic biosensors for food control. *Trends Food Sci. Technol.* **111**, 128–140 (2021). <https://doi.org/10.1016/j.tifs.2021.02.057>
13. P.R. Sahoo, P. Swain, S.M. Nayak, S. Bag, S.R. Mishra, Surface plasmon resonance based biosensor: A new platform for rapid

- diagnosis of livestock diseases. *Vet. World*. **9**, 1338–1342 (2016). <https://doi.org/10.14202/vetworld.2016.1338-1342>
14. S. Firdous, S. Anwar, R. Rafya, Development of surface plasmon resonance (SPR) biosensors for use in the diagnostics of malignant and infectious diseases. *Laser Phys. Lett.* **15** (2018). <https://doi.org/10.1088/1612-202X/aab43f>
  15. X. Shi, S. Zheng, H. Chi, X. Jin, X. Zhang, A wideband electro-optic modulator based on long range surface plasmon resonances. *J. Opt.* **13**, 11–16 (2011). <https://doi.org/10.1088/2040-8978/13/1/2/125001>
  16. L. Aprilia, D. Riana, W.P. Tresna, I. Tazi, R. Nuryadi, Surface Plasmon Resonance (SPR) Sensor for Measurement. *AIP Conf. Proc.* **3003**, 020106 (2024). <https://doi.org/10.1063/5.0186536>
  17. R. Kumar, S. Singh, H. Bouandas, J. Alam, Detection of COVID-19 using surface plasmon resonance sensor for sensitivity enhancement: theoretical analysis, plasmonics. (2025). <https://doi.org/10.1007/s11468-025-02762-6>
  18. H. Kushwah, J.K. Anand, A. Sachdeva, Enhancement of optical coupling efficiency of surface plasmon resonance based sensors. *IEEE Access*. **10**, 879–892 (2022). <https://doi.org/10.1109/ACCESS.2021.3137820>
  19. M.H. Elshorbagy, A. Cuadrado, J. Alda, High-sensitivity integrated devices based on surface plasmon resonance for sensing applications. *Photonics Res.* **5**, 654 (2017). <https://doi.org/10.1364/prj.5.000654>
  20. W.M. Mukhtar, P. Susthitha Menon, S. Shaari, M.Z.A. Malek, A.M. Abdullah, Angle shifting in surface plasmon resonance: experimental and theoretical verification. *J. Phys. Conf. Ser.* **431** (2013). <https://doi.org/10.1088/1742-6596/431/1/012028>
  21. J. Wang, A. Munir, Z. Zhu, H.S. Zhou, Magnetic nanoparticle enhanced surface plasmon resonance sensing and its application for the ultrasensitive detection of magnetic nanoparticle-enriched small molecules. *Anal. Chem.* **82**, 6782–6789 (2010). <https://doi.org/10.1021/ac100812c>
  22. Y. Xinglong, W. Dingxin, W. Xing, D. Xiang, L. Wei, Z. Xincheng, A surface plasmon resonance imaging interferometry for protein micro-array detection. *Sens. Actuators B Chem.* **108**, 765–771 (2005). <https://doi.org/10.1016/j.snb.2004.12.089>
  23. W.P. Hu, S.J. Chen, K.T. Huang, J.H. Hsu, W.Y. Chen, G.L. Chang, K.A. Lai, A novel ultrahigh-resolution surface plasmon resonance biosensor with an Au nanocluster-embedded dielectric film. *Biosens. Bioelectron.* **19**, 1465–1471 (2004). <https://doi.org/10.1016/j.bios.2003.12.001>
  24. P. Maurya, S. Maurya, R. Verma, Sensitivity enhancement of SPR based refractive index sensor in VIS-NIR region by using ZnS and PVP. *Results Opt.* **8**, 100246 (2022). <https://doi.org/10.1016/j.rio.2022.100246>
  25. A. Agharazy Dormeny, P. Abedini Sohi, M. Kahrizi, Design and simulation of a refractive index sensor based on SPR and LSPR using gold nanostructures. *Results Phys.* **16**, 102869 (2020). <https://doi.org/10.1016/j.rinp.2019.102869>
  26. X. Liu, L. Li, Y. Liu, X. Shi, W. Li, Y. Yang, L. Mao, Biosensors and bioelectronics ultrasensitive detection of deltamethrin by immune magnetic nanoparticles separation coupled with surface plasmon resonance sensor. *Biosens. Bioelectron.* **59**, 328–334 (2014). <https://doi.org/10.1016/j.bios.2014.03.020>
  27. B. Janani, A. Syed, A.M. Thomas, N. Marraiki, S. Al-Rashed, A.M. Elgorban, L.L. Raju, A. Das, S.S. Khan, Enhanced SPR signals based on Methylene diphosphonic acid functionalized Ag NPs for the detection of Hg(II) in the presence of an antioxidant glutathione. *J. Mol. Liq.* **311**, 113281 (2020). <https://doi.org/10.1016/j.molliq.2020.113281>
  28. S. Mohammadzadeh-Asl, A. Aghanejad, M. de la Guardia, J. Ezzati Nazhad Dolatabadi, A. Keshtkar, Surface plasmon resonance signal enhancement based on erlotinib loaded magnetic nanoparticles for evaluation of its interaction with human lung cancer cells. *Opt. Laser Technol.* **133**, 106521 (2021). <https://doi.org/10.1016/j.optlastec.2020.106521>
  29. A. Pal, A. Jha, A theoretical analysis on sensitivity improvement of an SPR refractive index sensor with graphene and barium titanate nanosheets. *Optik*. **231**, 166378 (2021). <https://doi.org/10.1016/j.ijleo.2021.166378>
  30. B. Hossain, I. Mustafa, M. Moznuzzaman, L. Faisal, A. Hossain, Results in physics high performance refractive index SPR sensor modeling employing graphene Tri sheets. *Results Phys.* **15**, 102719 (2019). <https://doi.org/10.1016/j.rinp.2019.102719>
  31. Y.A. Hong, J.W. Ha, Enhanced refractive index sensitivity of localized surface plasmon resonance inflection points in single hollow gold nanospheres with inner cavity. *Sci. Rep.* **12**, 1–9 (2022). <https://doi.org/10.1038/s41598-022-11197-6>
  32. T. Sun, Y. Zhang, F. Zhao, N. Xia, L. Liu, Self-assembled biotin-phenylalanine nanoparticles for the signal amplification of surface plasmon resonance biosensors. *Microchim. Acta.* **187** (2020). <https://doi.org/10.1007/s00604-020-04461-x>
  33. H. Chen, F. Qi, H. Zhou, S. Jia, Y. Gao, K. Koh, Y. Yin, Fe<sub>3</sub>O<sub>4</sub>@Au nanoparticles as a means of signal enhancement in surface plasmon resonance spectroscopy for thrombin detection. *Sens. Actuators B Chem.* **212**, 505–511 (2015). <https://doi.org/10.1016/j.snb.2015.02.062>
  34. K. Abdali, K.H. Abass, E. Al-bermany, E.M. Al-robayi, A.M. Kadim, Nano biomed eng of PVA / PAAM / PEO polymer blend doped with silver. *14* (2022) 114–122. <https://doi.org/10.5101/nbe.v14i2.p114-122.Abstract>
  35. S. Zhan, C. Li, H. Tian, C. Ma, H. Liu, J. Luo, M. Li, Synthesis, characterization and dye removal behavior of core-shell-shell Fe<sub>3</sub>O<sub>4</sub>/Ag/polyoxometalates ternary nanocomposites. *Nanomaterials*. **9**, 1255 (2019). <https://doi.org/10.3390/nano9091255>
  36. Q. Chen, Q. Wang, H. Wang, Q. Ma, Q. Chen, Surface plasmon resonance enhanced Faraday rotation in Fe<sub>3</sub>O<sub>4</sub>/Ag nanoparticles doped diamagnetic glass. *Plasmonics*. **13**, 163–174 (2018). <https://doi.org/10.1007/s11468-016-0496-7>
  37. M.P. Mcoyi, K.T. Mpofu, M. Sekhwama, P. Mthunzi-Kufa, Developments in localized surface plasmon resonance. *Plasmonics*. (2024) 3. <https://doi.org/10.1007/s11468-024-02620-x>
  38. X. Wang, X. Wang, Y. Liu, T. Chu, Y. Li, C. Dai, Y. Yang, Y. Zhang, Surface plasma enhanced fluorescence combined aptamer sensor based on silica modified silver nanoparticles for signal amplification detection of cholic acid. *Microchem. J.* **168**, 106524 (2021). <https://doi.org/10.1016/j.microc.2021.106524>
  39. D.I. Meira, A.I. Barbosa, J. Borges, V.M. Corrello, R.L. Reis, F. Vaz, Novel label-free localized surface plasmon resonance (LSPR) biosensor, based on Au-Ag NPs embedded in TiO<sub>2</sub> matrix, for on-site and sensitive detection of Ochratoxin-A (OTA) in wine. *Talanta*. **284** (2025) 127238. <https://doi.org/10.1016/j.talanta.2024.127238>
  40. J. Ding, Z. Liu, W. Li, C. Yin, H. Chen, Localized Surface Plasmon Resonance of Ag-SiO<sub>2</sub> Core-Shell Nanowire Tetramers. *Plasmonics*. (2025). <https://doi.org/10.1007/s11468-025-02802-1>
  41. M.K. Omar, N.M. Ahmed, A.A.M. Alqanoo, M.A. Almessiere, M.S.M. Abutawahina, E. Al-Bermany, Performance evaluation of aluminum nitride-decorated AgNWs-based transparent conductive electrodes deposited on flexible substrates. *J. Mater. Sci. Mater. Electron.* **35**, 1–10 (2024). <https://doi.org/10.1007/s10854-024-12211-5>
  42. A. Amirjani, D.F. Haghshenas, Sensors, B. Actuators, Chemical ag nanostructures as the surface plasmon resonance (SPR)-based sensors: A mechanistic study with an emphasis on heavy metallic ions detection. *Sens. Actuators B Chem.* **273**, 1768–1779 (2018). <https://doi.org/10.1016/j.snb.2018.07.089>
  43. S.D. Soelberg, R.C. Stevens, A.P. Limaye, C.E. Furlong, Surface plasmon resonance detection using antibody-linked magnetic nanoparticles for analyte capture, purification, concentration, and

- signal amplification. *Anal. Chem.* **81**, 2357–2363 (2009). <https://doi.org/10.1021/ac900007c>
44. R. Liang, G. Yao, L. Fan, J. Qiu, *Analytica chimica acta magnetic: Fe<sub>3</sub>O<sub>4</sub>@Au composite-enhanced surface plasmon resonance for ultrasensitive detection of magnetic nanoparticle-enriched  $\alpha$ -fetoprotein.* *Anal. Chim. Acta.* **737**, 22–28 (2012). <https://doi.org/10.1016/j.aca.2012.05.043>
  45. A.N. Dizaji, M. Yilmaz, E. Piskin, Silver or gold deposition onto magnetite nanoparticles by using plant extracts as reducing and stabilizing agents. *Artif. Cells Nanomed. Biotechnol.* **44**, 1–7 (2015). <https://doi.org/10.3109/21691401.2015.1019672>
  46. M. Riswan, N. Adrianto, I.M. Yahya, N.I. Istiqomah, A.M. Panre, S. Juharni, M. Wahyuni, I. Arifin, E. Santoso, Suharyadi, Effect of electric field on localized surface plasmon resonance properties of Fe<sub>3</sub>O<sub>4</sub>/Ag composite nanoparticles. *Optik.* **293**, 171404 (2023). <https://doi.org/10.1016/j.ijleo.2023.171404>
  47. W.M. Mukhtar, N.F. Murat, N.D. Samsuri, K.A. Dasuki, Maximizing the response of SPR signal: A vital role of light excitation wavelength. *AIP Conf. Proc.* **2016**, (2018). <https://doi.org/10.1063/1.5055506>
  48. W.M.A. Wan Ahamad, D. Kamarun, M.K. Abd Rahman, M.S. Kamarudin, Modular surface plasmon resonance (SPR) biosensor based on wavelength modulation. *Adv. Mater. Res.* **1107**, 699–705 (2015)
  49. X. Liu, D. Song, Q. Zhang, Y. Tian, L. Ding, H. Zhang, Wavelength-modulation surface plasmon resonance sensor. *TrAC Trends Anal. Chem.* **24**, 887–893 (2005). <https://doi.org/10.1016/j.trac.2005.05.010>
  50. S. Wahyuni, M. Riswan, N. Adrianto, M.Y. Dharmawan, R.M. Tumbelaka, R. Cuana, N.I. Istiqomah, A. Jiananda, S. Garcia, E. Suharyadi, Localized surface plasmon resonance properties dependence of green-synthesized Fe<sub>3</sub>O<sub>4</sub>/Ag composite nanoparticles on ag concentration and an electric field for biosensor application. *Photonics Nanostructures- Fundam Appl.* **57**, 101191 (2023). <https://doi.org/10.1016/j.photonics.2023.101191>
  51. X. Zhang, F. Zhang, J. Ren, Y. Wang, Z. Li, X. Li, Y. Wang, W. Zhao, W. Peng, Excitation-detection integrated trapezoidal prism-coupled surface plasmon resonance based on a compact optical system. *Sens. Actuators B Chem.* **427**, 137234 (2025). <https://doi.org/10.1016/j.snb.2025.137234>
  52. T.M.S. Ashrafi, G. Mohanty, Surface Plasmon Resonance Sensors: A Critical Review of Recent Advances, Market Analysis, and Future Directions. *Plasmonics.* (2025). <https://doi.org/10.1007/s11468-024-02740-4>
  53. M. Riswan, E. Widiyanto, N. Imani, C. Driyo, M. Arifin, I. Santoso, E. Suharyadi, Tuning optical properties of Au thin film using electric field for surface plasmon resonance biosensor application. *Opt. Mater.* **150**, 115221 (2024). <https://doi.org/10.1016/j.optmat.2024.115221>
  54. E. Widiyanto, N.M. Shobih, M.Y. Nursam, K. Hanna, A. Triyana, I. Rusydi, Santoso, Electronic correlations enhance optical absorption in graphene oxide-modified Methylammonium lead iodide perovskite. *J. Alloys Compd.* **947**, 169634 (2023). <https://doi.org/10.1016/j.jallcom.2023.169634>
  55. R.M. Kaloari, E. Widiyanto, I.K.A.P. Dana, A. Lukmantoro, E. Suharyadi, T. Kato, S. Iwata, M.U. Absor, I. Santoso, Anomalous optical properties of bismuth ultrathin film using spectroscopic ellipsometry in the visible - Ultraviolet range. *Thin Solid Films.* **773**, 139825 (2023). <https://doi.org/10.1016/j.tsf.2023.139825>
  56. P.D.J.I. Ketut Agus, E. Putra Dana, I. Suharyadi, Santoso, A compact modular multi-wavelength (200-850nm) rotating-analyzer ellipsometer for optical constant characterization of nanostructured materials. *Eur. J. Phys.* **41**, 1–6 (2022). <https://doi.org/10.1088/1361-6404/ab9b3e>
  57. H. Fujiwara, Spectroscopic ellipsometry: principles and applications, *spectrosc. Ellipsom Princ Appl.* 1–369 (2007). <https://doi.org/10.1002/9780470060193>
  58. H. Fujiwara, R.W. Collins, Spectroscopic ellipsometry for photovoltaics 2: applications and optical data of solar cell materials, 214 (2018). <https://link.springer.com/book/10.1007/978-3-319-95138-6>
  59. R.A.N. Khasnaah, A. Herawati, L.Z. Maulana, E.A. Suyono, E. Suharyadi, I. Santoso, T. Kato, S. Iwata, Spectroscopic ellipsometry based biosensor on gold thin film for detection of microalgae. *Key Eng. Mater.* **840**, 412–417 (2020). <https://doi.org/10.4028/www.scientific.net/kem.840.412>
  60. J. Toudert, R. Serna, C. Deeb, E. Rebollar, Optical properties of bismuth nanostructures towards the ultrathin film regime. *Opt. Mater. Express.* **9**, 2924 (2019). <https://doi.org/10.1364/ome.9.002924>
  61. G. Orozco-Hernández, J. Olaya-Flórez, C. Pineda-Vargas, J.E. Alfonso, E. Restrepo-Parra, Structural, chemical and electrochemical studies of bismuth oxide thin films growth via unbalanced Magnetron sputtering. *Surf. Interfaces.* **21**, 100627 (2020). <https://doi.org/10.1016/j.surfin.2020.100627>
  62. Q. Fu, Radiation transfer in the atmosphere: cloud-radiative processes. *Encycl Atmos. Sci. Second Ed.* **5**, 13–15 (2015). <https://doi.org/10.1016/B978-0-12-382225-3.00338-8>
  63. F.D. Laksono, M. Supardianningsih, K. Arifin, Abraha, Development of low cost and accurate homemade sensor system based on surface plasmon resonance (SPR). *J. Phys. Conf. Ser.* **1011**, 012043 (2018). <https://doi.org/10.1088/1742-6596/1011/1/012043>
  64. E. Al-Bermamy, A.T. Mekhalif, H.A. Banimuslem, K. Abdali, M.M. Sabri, Effect of green synthesis bimetallic Ag@SiO<sub>2</sub> core-shell nanoparticles on absorption behavior and electrical properties of PVA-PEO nanocomposites for optoelectronic applications. *Silicon.* **15**, 4095–4107 (2023). <https://doi.org/10.1007/s12633-023-02332-7>
  65. S. Kosame, M.J. Josline, J.H. Lee, H. Ju, Anomalous spectral shift of localized surface plasmon resonance. *Nanoscale Adv.* **6**, 2636–2643 (2024). <https://doi.org/10.1039/d3na01131c>
  66. T.J. Wang, C.W. Hsieh, Phase interrogation of localized surface plasmon resonance biosensors based on electro-optic modulation. *Appl. Phys. Lett.* **91**, 89–92 (2007). <https://doi.org/10.1063/1.2783213>
  67. S.A. Abayzeed, R.J. Smith, K.F. Webb, M.G. Somekh, C.W. See, Sensitive detection of voltage transients using differential intensity surface plasmon resonance system. *Opt. Express.* **25**, 31552 (2017). <https://doi.org/10.1364/oe.25.031552>
  68. B.E.A. Saleh, M.C. Teich, *Fundamentals of Photonics*, second edn. (Wiley, 2007), pp. 1114–1115. <https://doi.org/10.1002/0471213748>
  69. M. Riswan, M. Arifin, I. Santoso, K. Nawa, K. Nakamura, E. Suharyadi, Effect of change in number of electrons to optical properties and surface plasmon resonance of noble metals. *Comput. Mater. Sci.* **247**, 113519 (2025). <https://doi.org/10.1016/j.commatsci.2024.113519>
  70. B.H. Ong, X. Yuan, S.C. Tjin, J. Zhang, H.M. Ng, Optimised film thickness for maximum evanescent field enhancement of a bimetallic film surface plasmon resonance biosensor. *Sens. Actuators B Chem.* **114**, 1028–1034 (2006). <https://doi.org/10.1016/j.snb.2005.07.064>
  71. S. Priya, R. Laha, V.R. Dantham, Wavelength-dependent angular shift and figure of merit of silver-based surface plasmon resonance biosensor. *Sens. Actuators Phys.* **315**, 112289 (2020). <https://doi.org/10.1016/j.sna.2020.112289>
  72. J.W. Jeon, P.A. Ledin, J.A. Geldmeier, J.F. Ponder, M.A. Mahmoud, M. El-Sayed, J.R. Reynolds, V.V. Tsukruk, Electrically Controlled Plasmonic Behav. *Gold. Nanocube@Polyaniline*

- Nanostructures: Transparent Plasmonic Aggregates *Chem. Mater.* **28**, 2868–2881 (2016). <https://doi.org/10.1021/acs.chemmater.6b00882>
73. P.A. Ledin, J.W. Jeon, J.A. Geldmeier, J.F. Ponder, M.A. Mahmoud, M. El-Sayed, J.R. Reynolds, V.V. Tsukruk, Design of hybrid electrochromic materials with large electrical modulation of plasmonic resonances. *ACS Appl. Mater. Interfaces.* **8**, 13064–13075 (2016). <https://doi.org/10.1021/acsami.6b02953>
74. S. Gupta, A. Paliwal, V. Gupta, M. Tomar, Waveguide coupled surface plasmon resonance based electro optic modulation in SBN thin films. *Appl. Surf. Sci.* **458**, 139–144 (2018). <https://doi.org/10.1016/j.apsusc.2018.07.039>
75. L. Ma, S. Xu, C. Wang, H. Wang, S. Zou, M. Su, Electrically modulated localized surface plasmon around self-assembled-monolayer-covered nanoparticles. *Langmuir.* **33**, 1437–1441 (2017). <https://doi.org/10.1021/acs.langmuir.6b03537>
76. T.J. Wang, P.C. Ho, Localized surface plasmon resonance biosensing by electro-optic modulation with sensitivity and resolution tunability. *J. Appl. Phys.* **109**, 064703 (2011). <https://doi.org/10.1063/1.3563065>
77. K.C. Hsieh, H.L. Chen, D.H. Wan, J. Shieh, Active modulation of surface plasmon resonance wavelengths by applying an electric field to gold nanoparticle-embedded ferroelectric films. *J. Phys. Chem. C* **112**, 11673–11678 (2008). <https://doi.org/10.1021/jp711828k>
78. S.-C. Ma, R. Gupta, N.A.P. Ondevilla, K. Barman, L.-Y. Lee, H.-C. Chang, J.-J. Huang, Voltage-modulated surface plasmon resonance biosensors integrated with gold nanohole arrays. *Biomed. Opt. Express.* **14**, 182 (2023). <https://doi.org/10.1364/boe.478164>

**Publisher's note** Springer Nature remains neutral with regard to jurisdictional claims in published maps and institutional affiliations.

Springer Nature or its licensor (e.g. a society or other partner) holds exclusive rights to this article under a publishing agreement with the author(s) or other rightsholder(s); author self-archiving of the accepted manuscript version of this article is solely governed by the terms of such publishing agreement and applicable law.